Colloidal Dynamics in Evanescent Optical Fields

A Thesis

submitted to
Indian Institute of Science Education and Research, Pune
in partial fulfilment of the requirements for the MS degree Programme
by

Chaudhary Eksha Rani

Indian Institute of Science Education and Research, Pune
Dr. Homi Bhabha Road,
Pashan, Pune 411008, INDIA

May, 2024

Supervisor: Dr. G. V. Pavan Kumar

Certificate of Examination

This is to certify that this dissertation entitled ”Colloidal Dynamics in Evanescent Fields” towards the partial fulfilment of the MS degree programme at the Indian Institute of Science Education and Research, Pune, represents the study/work carried out by Chaudhary Eksha Rani (Reg. no. 20212024) at Indian Institute of Science Education and Research Pune under the supervision of Prof. G V Pavan Kumar, Department of Physics, during the academic year 2023-2024.

Thesis Committee Members

Prof. G V Pavan Kumar
Dr. Vijayakumar Chikkadi

Prof. G V Pavan Kumar
(Supervisor)

Dated: 15th March, 2024

Declaration

I hereby declare that the matter embodied in the report titled "Colloidal dynamics in evanescent fields" are the results of the work carried out by me at the Department of Physics, Indian Institute of Science Education and Research (IISER) Pune, under the supervision of Prof G V Pavan Kumar, and the same has not been submitted elsewhere for any other degree. Wherever others contribute, every effort is made to indicate this clearly, with due reference to the literature and acknowledgement of collaborative research and discussions.

Chaudhary Eksha Rani

Roll No. 20212024

Dated: 15th March 2024

Acknowledgements

Firstly, I would like to thank my supervisor, Prof G V Pavan Kumar, for his invaluable guidance and support throughout my MS and this thesis. His mentoring has played a major role in shaping this work and my scientific skills to its current state. He has always motivated me to work with "constancy and moderation" in whatever task I pursue. Inculcating this strategy into my research while working under his supervision has proven to be a skill of paramount importance, which has facilitated the culmination of this thesis.

I am extremely grateful for the support I have received from my colleagues- Rahul, Diptabrata, Ashutosh, Sunny, Shailendra, Vandana, Sumant and Sneha. Especially, I would like to thank Rahul and Diptabrata from whom I received a majority part of my experimental training and from whom I learnt the "scientific" way of thinking, which will continue to benefit me throughout my research career. I thank Sunny and Shailendra for helping me in the initial stages of the experiments and giving their time to help solve the difficulties I faced. Ashutosh gave crucial inputs to the thermoelectric part of this work and helped me with the spectral measurements, which gave an additional angle to this thesis and I thank him for that. I would also like to thank Sagnik for gold thickness measurement using reflection spectroscopy, and the very interesting optics experimentation discussions we had.

A very special thanks to all my beautiful friends on the campus, who helped me maintain my enthusiasm and calm in times of difficulties. Especially a special mention to Eishica, also my colleague from the first year in the lab, who made me laugh even on days when my obvious experiments would fail and encouraged me to try again and keep trying while keeping a smile. I thank Arindam, the familiar face in $\hbar$ from across the corridor, who helped me through some difficult times and kept my morale high with endless motivation.

Finally, I would like to thank Mritunjay, my best friend in another country, who has been my strongest pillar of strength throughout my years in IISER. Despite the virtual presence, his unconditional support and faith have been the most crucial in challenging times, encouraging me to believe in my abilities, give myself and my experiments another try and not be shot down by a few negatives.

And ofcourse, last but most important, I thank my family, especially my mother, for the comfort I received from her each day, charging me up for another day in the campus. This work would not have been possible without them.

Abstract

Reversible particle assemblies are of great interest to researchers working in the fields of nanotechnology, biochemistry and materials science. Assemblies of nanoparticles have been achieved using surface plasmon excitations facilitated by evanescent illumination. Such mechanisms utilise the plasmon-mediated heat to drive fluid flow, which leads to particle accumulation. In this thesis, we study in detail to decouple the effects of these fields and forces involved in the formation of large-scale nanoparticle assemblies. We quantify and draw a contrast between the role of optical (plasmonic) and fluidic fields, showing the dominance of fluidic effects by a huge margin. Once their significance and strength are established, we add a component of an even stronger field called the thermoelectric field, facilitated by the addition of an electrolyte, which generates an electric field under temperature gradients. We compare the assemblies formed with only the plasmofluidic field and that, in the presence of thermoelectric fields and demonstrate a multifold intensity enhancement in the latter case. This work will have applications in studying scattered light signatures from highly scattering particle assemblies and biosensing, like SERS, at relatively lower powers. Experimental observations are accompanied by extensive simulation analysis in finite element method-based COMSOL.

List of Figures

List of Tables

Contents

Chapter 1

INTRODUCTION

Colloidal particles exhibit Brownian motion, which refers to the random movement of particles in a fluid medium [1]. Their dynamics can be manipulated using electromagnetic fields [2], hydrodynamic forces [3], chemical treatment [4], etc, by driving the system out-of-equilibrium. This can lead to emergent phenomena like the self-assembly of colloids [5][6], pattern formation [7], and directed diffusion [8], among others. Reversible self-assembly is of particular interest in the field of nanotechnology [9][10] and biosensors [11] [12], one of the applications of which is light manipulation using nanofabricated structures [13]. If the self-assembling units are plasmonic in nature, light can be tailored at subwavelength scales. Assemblies of chemically functionalised nanoparticles are an attractive option for researchers in the field of biotechnology to interact with and generate responses in biological systems [14][15]. Optical fields are a convenient way to manipulate such colloidal dynamics, while also facilitating other mediated effects like opto-thermal [16], opto-fluidic [3], and opto-thermoelectric [17], to name a few. Not only is it possible to manipulate colloidal dynamics using light, but it is also possible for the colloids to manipulate the light itself [18]. Metallic nanoparticles, which are capable of exciting plasmons, are famous for their ability to localise light and lead to field enhancement. This gives rise to further unique optical properties and interparticle interactions [19][20].

However, it is challenging to control the dynamics of nanoparticles owing to their strong Brownian nature and extremely small volume. While single nanoparticle manipulation has been achieved, it requires the use of highly focused optical beams with large power gradients and optically mediated external mechanisms like fluid flow [3]. Manipulation and control of nanoparticles on a large scale in a reversible manner is further challenging using focused optical tweezers. In such cases, evanescent excitation can serve the purpose of large-scale illumination [20]. It can be used to excite plasmonic fields, which can influence particle dynamics effectively on a much larger scale at lower laser intensities. Such

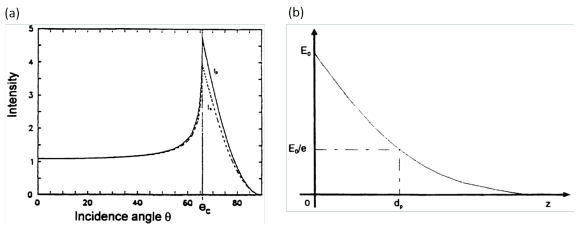

Figure 1.1: (a) Variation of intensity in the rarer medium vs incident angle for a glass-water interface ($n_1 = 1.46$, $n_2 = 1.33$) (b) Exponential decay of electric field amplitude with distance from the surface in the rare medium [23].

plasmonic traps work in conjunction with the heat-mediated fluid flow due to plasmon excitation and are thus referred to as plasmofluidic traps [6]. They are a powerful option to manipulate the colloidal dynamics of particles down to the size of a few hundred nanometers over a large scale despite their Brownian motion. In this thesis, we aim to understand the mechanism of such plasmofluidic traps in controlling nanoparticle dynamics and how they can be strengthened with additional components like thermoelectric fields [21][22]. In this chapter, we summarise some preliminary concepts that will be used to understand the principles used in this work.

1.1 Evanescent field

Consider an electromagnetic plane wave incident on an interface between two media of refractive indices n_1 and n_2 where $n_1 > n_2$, that is, light is incident on a denser-to-rarer interface. If the angle of incidence is greater than the critical angle $\theta_c = sin^{-1}(n_2/n_1)$, then the electromagnetic wave gets totally internally reflected into denser medium n_1. Upon solving Maxwell's equations for this electromagnetic wave at the interface, taking into account the boundary conditions and continuity equations, it is found that, in the rarer medium, the amplitude of the field decreases exponentially as the distance from the interface increases. The intensity of the transmitted wave also depends on the angle of incidence and the incident polarization. The plane wave having the electric field polarised in the plane of incidence is called transverse magnetic (TM) or p-polarised, and that polarised perpendicular to the plane of incidence is called transverse electric (TE) or s-polarised. The intensity vs incident angle is plotted for both polarisations for a glass-water interface, as shown in Fig 1.1 [23]. The distance from the interface where the amplitude decays to 1/e of the amplitude at the interface is called the penetration depth of the evanescent field. It is a measure of confinement of the evanescent field and is given as [24]

$$d_p = \frac{\lambda}{2\pi\sqrt{n_1^2 sin^2\theta - n_2^2}}. \tag{1.1}$$

As indicated by the equation, it depends on the incident wavelength, angle of incidence and also on the refractive index contrast between the two media.

1.2 Evanescently excited surface plasmons

Surface plasmons (SP) are surface waves, propagating along a conducting surface, that arise due to the collective oscillation of the free electrons in the conductor with the electromagnetic light wave. One of their unique properties is their ability to confine light in very localised spots, giving enhanced intensity, which has direct applications in fluorescence and sensing experiments. When the Maxwell's equations are solved taking into account the lossy nature of the conducting medium, it is found that SPs have a greater momentum than the free-space photon of the same frequency [13].

$$k_{SP} = k_0\sqrt{\frac{\varepsilon_d\varepsilon_m}{\varepsilon_d + \varepsilon_m}} \tag{1.2}$$

Where, k_0 is the wave vector of electromagnetic wave in vacuum, ε_d and ε_m are frequency-dependent relative permittivity of dielectric and metal respectively. Due to this mismatch in momentum, SPs are confined to the surface of the conductor and can be used, for example, to guide the light in miniaturised photonic circuits. As a consequence, SPs intensity decays exponentially away from the metal surface and they are said to be evanescent in nature. To be able to excite SPs, ε_m must be negative, which is true for all metals since they have a negative and complex permittivity. Due to a momentum mismatch between the incident wave and SPs, they cannot be excited by direct illumination. To compensate for the extra momentum, one can either use prism coupling or scattering from a topological defect or periodically structured metal surface like a grating. In this work, we use prism coupling to excite surface plasmons on a metal surface, which is chosen to be a thin film of gold (Au).

The prism coupling can again be of two types [25]:

1. Otto configuration: The metal film is kept very close to the TIR surface of the prism, forming an air gap. When light undergoes TIR, the evanescent waves tunnel through the airgap and excite SPs on the bottom metal surface.

2. Kretschmann configuration: The metal film is effectively in contact with the TIR surface of the prism. When light undergoes TIR, the evanescent waves directly excite the SPs in the upper surface of the metal film.

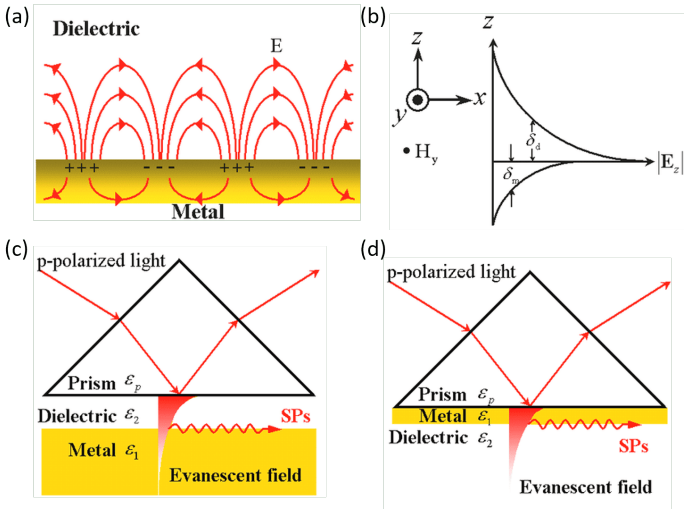

Figure 1.2: (a) Surface plasmons at the metal-dielectric interface have combined electromagnetic wave and surface charge charecteristics. The SPs are confined to the interface, propagating along and decaying perperndicular to it. (b) Decay in the electric field magnitude into the metal and dielectric media. (c) Otto configuration and (d) Kretschmann configuration to excite surface plasmons on a metal film [25].

In this work, we use the Kretschmann configuration to excite surface plasmons on the top surface of a thin Au film. The excitation of surface plasmons is very sensitive to the incident polarisation and incident angle. Upon solving Maxwell's equations with appropriate boundary and continuity equations, it is found that TE modes cannot excite surface plasmons, that is, the light must be p-polarised (electric field in the plane of incidence) to be able to excite surface plasmons. When the incident light falls at the resonant angle, then maximum energy of the incident wave is coupled to the SP. This is confirmed by measuring the reflectivity from the prism, which exhibits a minimum at the SP resonance angle. This is called surface plasmon resonance (SPR) and occurs when the momentum of the evanescent wave matches that of the surface plasmon, and the incident angle is [26]

$$\theta_{SPR} = sin^{-1}\left(\frac{1}{n_1}\sqrt{\frac{n_2^2 n_1^2}{n_2^2+n_1^2}}\right) \tag{1.3}$$

However, in our experimental arrangement, as described in the next chapter, due to the absence of control over incident angle, the resonant excitation of surface plasmons is not possible. This means that not all of the incident energy is converted into SP.

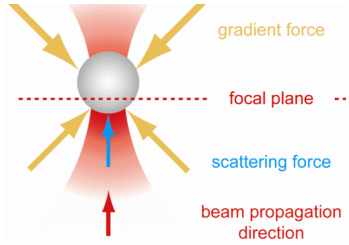

Figure 1.3: Schematic of optical gradient and scattering forces on a spherical particle [28].

1.3 Surface plasmon mediated effects

1.3.1 Optical forces

From the solution of Maxwell's equations, it is obtained that SP electromagnetic waves propagate along the surface and decay exponentially perpendicular to it. No energy is transferred into the rarer medium and it is only confined to propagate along the interface. Being electromagnetic waves, SPs have the ability to exert optical forces on matter that interacts with them. Since they are evanescent waves, these forces are stronger when the object is closer to the surface, where its volume overlaps with the field. It is known that a focused optical field exerts gradient and scattering forces, also called radiation pressure, on a spherical dipolar particle, given as [27]

$$F_{grad} = \frac{1}{4}\frac{Re\{\alpha_d\}}{c\varepsilon_0}\nabla I_i \tag{1.4}$$

$$F_{scat} = \frac{\sigma_{ext}}{c}S_i \tag{1.5}$$

Where, α_d is the complex polarisability of particle, I_i is the intensity of electromagnetic wave, σ_{ext} is the extinction cross-section of the particle and S_i is the time-averaged poynting vector of the electromagnetic wave. While the gradient force pushes the particle along the intensity gradient into the focused spot, the scattering force pushes it out of the focal plane along the propagation direction, as shown in Fig 1.3 [28]. As a combined effect, the particle settles in an off-centred position with respect to the focus where the net force on the particle is minimum and the scattering and gradient force components are balanced. SPs are complex electromagnetic waves and the particles used in our study are not spherical dipolar. Thus, the general approach of calculating the optical forces using the Maxwell stress tensor (MST) is used. Broadly, radiation pressure has a gradient-force like component that pulls the particle into the high intensity region and a scattering force component that pushes the particle along propagation direction of the wave.

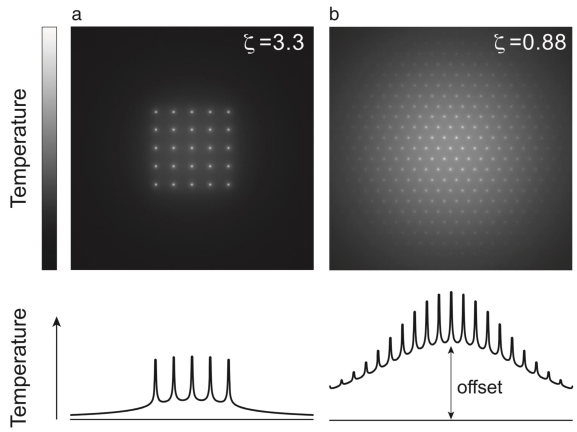

Figure 1.4: Temperature profile for an array of nanoparticles in the (a) localisation and (b) homogenisation regimes [29].

1.3.2 Heating of metal

Plasmonic heating is an integral part of this work. Upon illumination, the free charges in the metal film will oscillate at the frequency of the incident light, which will cause energy dissipation via the Joule effect. The metal film can be thought of as a uniform distribution of metal nanoparticles of thermal conductivity κ. These particles can be thought of as being embedded between two dielectric media, like glass and water in our case. Then κ_s is the average thermal conductivity of these media. Each nanoparticle will deliver a heat power Q given as [29]

$$Q = \frac{\omega}{2}\varepsilon_0 Im(\varepsilon_\omega)\int_V |E_\omega|^2 dr \tag{1.6}$$

Where ω is the angular frequency of illumination, ε_ω is the electric permittivity of the nanoparticle at frequency ω, and the integral is over the volume V of the nanoparticle. Then, the temperature distribution generated will be

$$T(r) = \frac{Q}{4\pi\kappa r} + T_\infty \tag{1.7}$$

Here, T_∞ is the temperature at an effectively infinite distance from the nanoparticle. Now, if N such identical nanoparticles are delivering power Q each, then the temperature increase anywhere in the surrounding medium will be

$$\delta T(r) = \sum_{k=1}^{N} \frac{Q_k}{4\pi\kappa_s |r - r_k|} \tag{1.8}$$

The total temperature originates from the self-heating of each nanoparticle, δT_{self}, and the external temperature rise contributed by all other neighbouring particles, δT_{ext}. Total temperature rise at a point is thus $\delta T_j = \delta T_{self} + \delta T_{ext}$. Depending on the relative strength

of these two contributions, there are two regimes: if δT_{self} dominates, then the temperature confinement regime and if δT_{ext} dominates then temperature homogenization occurs. For a 2D distribution of nanoparticles of size L, average interparticle distance p, and particle radius a, as an approximation to a thin metal film, the dimensionless parameter deciding the temperature regime is $\zeta_m = p^2/3La$. If $\zeta_m << 1$, then thermal collective effects will lead to a fully smooth temperature distribution. For a thin metal film, considered as a close-packed array of nanoparticles, $p << a << L$ which will give $\zeta_m << 1$ and thus a smooth temperature profile. On the contrary, if $\zeta_m >> 1$, in the localisation regime, the temperature distribution will exhibit hotspots around each nanoparticle location, as shown in Fig 1.4.

1.4 Temperature mediated effects

The temperature rise facilitated by the excitation of surface plasmons on a metal film can induce temperature gradient in the system. Depending on the surrounding medium, these gradients can lead to some interesting consequences [30]. In the presence of a fluid, the temperature gradients can lead to fluid flow. If the fluid is an electrolyte, then the temperature gradients can also lead to ionic concentration gradients.

1.4.1 Fluid flow

The temperature gradient in the system can lead to natural convective fluid flow due to temperature-dependent density variations [31]. Note that convective flow can exist even in the absence of any colloids in the solution. Convective flows generated by heating sub-wavelength metallic structures are only a few nm/s. It is also very sensitive to the height of the fluid column since that determines the vertical temperature gradients. For very small heights, the convective flow can be largely suppressed and regarded as negligible.

Another type of fluid flow arises due to temperature-dependent interfacial interaction energies, called the slip fluid flow [32]. A temperature gradient along the surface can lead to different interaction energies between the fluid and solid at different points on their surfaces. This leads to a boundary layer flow, of the order of sub-$\mu m/s$, along the interface corresponding to the length scale of the liquid-solid interaction. Slip fluid flow along a particle-fluid interface can give rise to phoretic motions like thermophoresis and diffusiophoresis, as shown in Fig 1.5[18]. In case of thermophoresis, the particle velocity u is characterised by its thermodiffusion coefficient D_T as $u = D_T \nabla T$. A general description of thermophoresis of a particle is given by the parameter called Soret coefficient $S_T = D_T/D$ where D is the Brownian diffusion coefficient of the particle. $S_T > 0$ implies that the particle

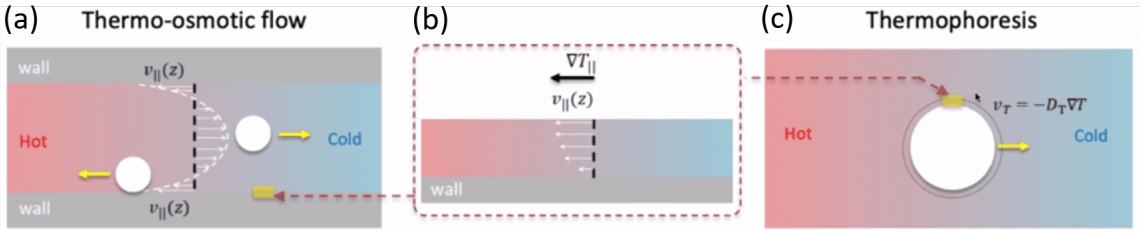

Figure 1.5: (a) Colloidal particles under the effect of a temperature gradient will either migrate to the hot or to the cold side depending on the solid-liquid interfacial interaction, which determines their Soret coefficient. (b) Thermo-osmotic slip flow in a boundary layer at the solid-liquid interface. (c) Thermo-osmotic flow along the particle surface lead to thermophoretic motion [18].

is thermophobic and $S_T < 0$ implies that the particle is thermophilic.

1.4.2 Thermoelectric field

If the sample solution is electrolytic, that is, it contains ions, then a temperature gradient in the solution can lead to thermophoretic migration of the ions. Depending on the mass, diffusion coefficient, and thermodiffusion coefficient of the ions, it is possible that cationic and anionic species exhibit different degrees of thermophoretic motion. That is, they can move with different velocities and in different directions till a steady state is reached. Ultimately, this can lead to a spatial separation of the ions in the solution, inducing an electric field which is directed along the temperature gradient. Such an electric field generated due to thermal gradients is termed as thermoelectric field. This field can exert force on a charged particle, the magnitude of which will depend on the charge and the electric field itself, which is given by the following equation [17],

$$E_T = \frac{k_B T \nabla T}{e} \frac{\sum_i Z_i n_i S_{Ti}}{\sum_i Z_i^2 n_i} \tag{1.9}$$

where for an ion i, Z_i is the charge on the ion and n_i is the concentration of the ion.

1.5 Problem at hand

Colloidal dynamics in evanescent fields have been studied in great detail. As described before, evanescent fields can be used to excite surface plasmons on a metal surface. Scientists have studied the effects of surface plasmon fields on colloidal dynamics, leading to the formation of colloidal assemblies, directed motion, and optical binding of arrays, among others. Focusing on colloidal assemblies, dielectric colloids are relatively easy to

assemble and form close-packed structures. Less power is required, and their assembly can be directly controlled using their temperature-dependent thermophoretic response. On the other hand, plasmonic particles are challenging to assemble in close packing. Large-scale manipulation of metallic particles, especially nanoparticles, is difficult to achieve with conventional optical tweezing methods. Owing to their large scattering cross-section, they are tough to trap under standard focused optical potentials. Plasmonic particle trapping is also sensitive to the plasmonic resonance of the particle, due to which a single wavelength laser cannot be used to trap nanoparticles of different sizes. Trapping under a focused laser also heats up the nanoparticles which leads to strong temperature gradients and consequent fluid flows, further making the trap unstable.

Evanescently excited surface plasmons provide a solution to trap and manipulate plasmonic nanoparticles on a large scale, without worrying about their plasmonic resonances or large scattering cross-sections. Here, we will study in detail the mechanism of such traps, which are not purely optical but optically-assisted. The role of thermal and fluidic fields is dominant is such traps, due to which they are often termed as thermofluidic potentials. Since SP fields generate the thermal gradients, they are also called plasmofludic potentials. These potentials can further be made stronger and more effective, especially for smaller nanoparticles, by the addition of an electrolyte and, thus, a thermoelectric field. In this thesis, we aim to study the extent of the role played by each of the optical, thermal, fluidic and thermoelectric fields in the manipulation of colloidal dynamics, composed of nanoparticles, over a large scale.

In this chapter, we touched upon the pre-requisite concepts required for this study. Chapter 2 talks about the experimental and simulation methods used in this study, including sample preparation. Chapter 3 discusses the experimental results and interpretations. In the end, we conclude with Chapter 4, mentioning the scope and significance of the results derived from this work.

Chapter 2

EXPERIMENTAL AND NUMERICAL METHODS

2.1 Sample Preparation

2.1.1 Colloidal solution

In this work, we use gold nanoparticles (AuNP) of varied sizes: 400 nm, 250 nm, and 150 nm in diameter. Although their geometry has facets, they are approximated to be spherical. These particles are commercially bought and dispersed in a citrate buffer. One mL of the buffer solution is centrifuged for 5 minutes so that nanoparticles get collected at the bottom of the centrifuge tube, the citrate solution is pipetted out and 1 mL milliQ water is added. This is repeated three times in total to rinse the particles and get a 1 mL AuNP solution in milliQ water. Since the particle density is very high, the solution is diluted to half by adding another 1 mL of milliQ water.

2.1.2 Thin film preparation

To facilitate surface plasmon excitation, a thin gold (Au) film is deposited on a glass coverslip using thermal vapour deposition (TVD). The coverslips to be coated are fixed on the sample holder inside the TVD chamber. The boats are loaded with sufficient Au and chromium (Cr) and placed between the electrodes. The vacuum pump is turned on, and the coating is started at a pressure of $\sim 10^{-5}$ mbar. First, a thin 5 nm Cr layer is coated to ensure effective adhesion of Au onto the coverslip. Following this, 50 nm of Au is coated. After the deposition, the TVD chamber is vented, and samples are collected. The thickness of the Au film is measured using reflection spectroscopy, giving a thickness of ~ 51 nm.

2.1.3 Preparation of sample chamber

Before every experiment, the Au film is washed with isopropanol (IPA), acetone and ethanol in this order. The experiments are performed in a thin fluid column. For this, a moderately concentrated solution of 10 µm SiO_2 particles in ethanol is prepared. A few microliters of this solution are drop-casted into a square boundary on the Au film and left to dry so that a square region is formed. Then, this boundary is coated with a thin layer of PDMS (SYLGARD 184), acquired from Sigma-Aldrich, for sealing the sample chamber. Finally, 3 µL of AuNP solution is pipetted in the middle of the square region, and another coverslip, cleaned with acetone, is placed on top, as shown in Fig 2.1. This forms a sample chamber of height 10 µm, due to colloids at the boundary, sealed by PDMS.

2.2 Experimental setup

To excite surface plasmons on the Au film, we construct the Kretschmann configuration on an upright microscope assembly, as shown in Fig 2.1. A 532 nm CW Gaussian laser beam is aligned and allowed to pass through a combination of half-waveplates and polarisers. This is done to control the polarisation and intensity of the incident beam. A dove prism (10 mm, ThorLabs, refractive index = 1.52) is placed on the microscope stage. The laser enters the prism horizontally and gets totally internally reflected (TIR) at its top surface. Given the geometrical design of the prism (acute angles = 45^o) and its optical properties, a ray of light entering one of the slant faces horizontally will undergo TIR by default since the angle of incidence at the glass-water interface (72.75^o) will be greater than the critical angle ($\theta_c \sim 61.1^o$).

At the top surface of the prism, a drop of index-matching oil (refractive index = 1.518) is poured, and the sample prepared on the Au-coated coverslip is mounted. This is done to avoid the formation of an extra air-glass interface, which ensures that the light exiting from the top surface of the prism undergoes refraction only at the glass-water interface. The scattered light from the surface is then collected from an objective lens - 4x NA = 0.13, 40x NA = 0.65, 100x NA = 0.95 and imaged in the real plane or the Fourier plane. A real image of the evanescently excited surface plasmon spot on the Au surface, in a thin chamber geometry, is shown in Fig 2.2, viewed under the 4x objective lens. The length of the excitation spot spans $\sim$ 400 µm and width of $\sim$ 100 µm. For spectral measurements, the light is redirected to the spectrometer. A 532 nm long pass filter is also placed in the path to block the excitation wavelength. The range of powers used lies between 5 mW to 45 mW.

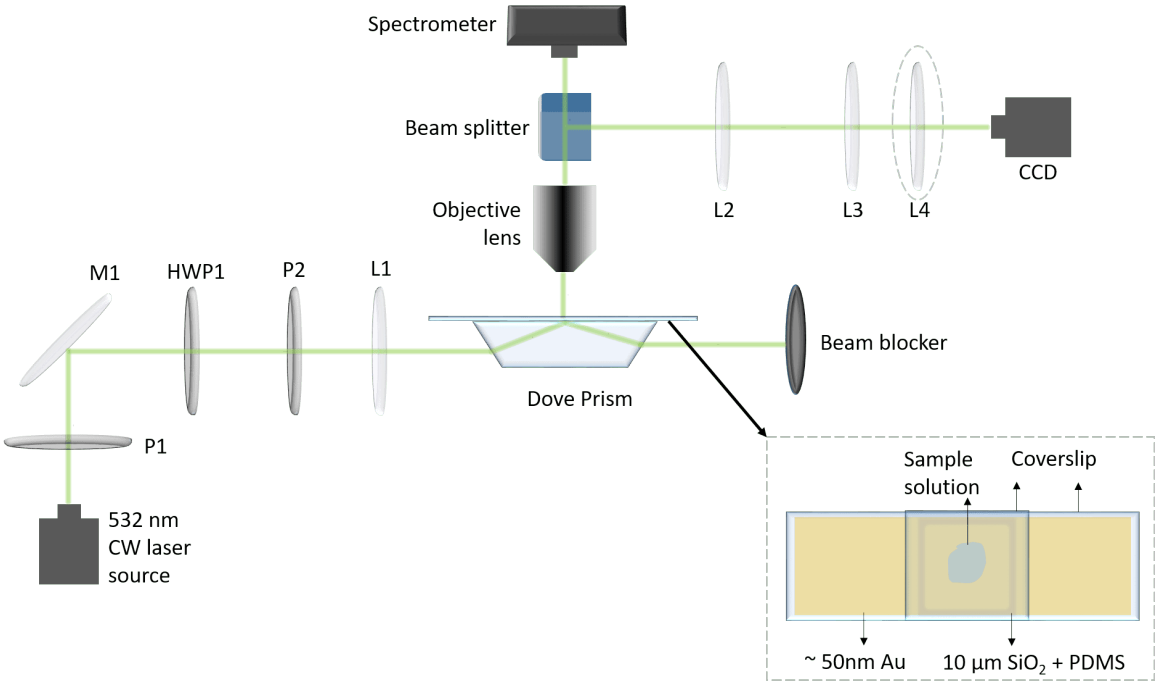

Figure 2.1: Experimental setup. A continuous wave (CW) 532 nm Gaussian laser beam passes through a polariser P1 to fix its polarisation plane. After being reflected by mirror M1, it passes through a series of half waveplate HWP1 and polariser P2 which gives direct control over its polarisation and intensity. A lens L1 of focal length 150 mm is used to loosely focus the laser at the top interface of the dove prism, where it gets totally internally reflected. The scattered light from the coverslip, kept on the dove prism after using an index matching oil, is collected by an objective lens of 4x, NA $= 0.13$ or 40x NA $= 0.65$. The light is then directed to a spectrometer and the CCD via a beamsplitter. L2 ($f = 150$ mm) and L3 ($f = 75$ mm) combination projects the Fourier image whereas L2, L3, L4 ($f = 50$ mm) combination projects the real image on the CCD.

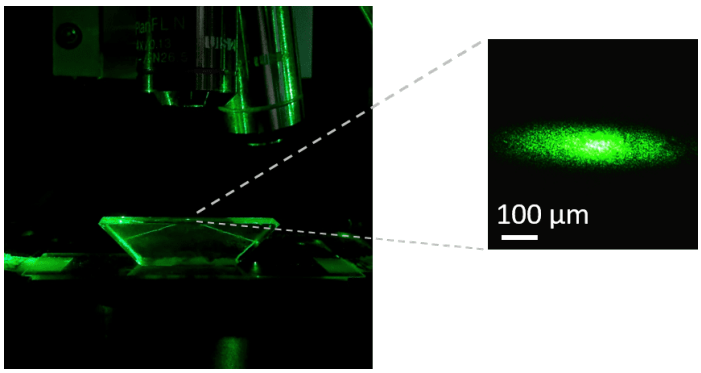

Figure 2.2: Image depicting total internal reflection inside the prism. Inset shows formation of a bright evanescent spot at the centre on the top surface, as viewed using a CCD.

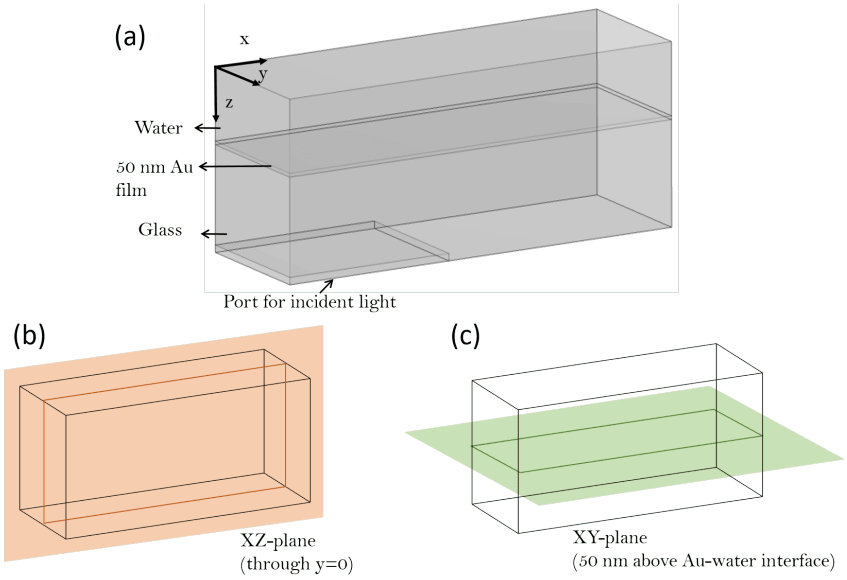

Figure 2.3: (a) Geometry used for COMSOL simulations. All computed quantities, like the electric field, temperature, and fluid flow, are plotted in the cross-section XZ and XY planes, as shown in (b) and (c).

Given the large spatial extent of the excitation spot, the resultant intensity lies in the range $8.5 - 76.4 \times 10^{-5}$ mW/μm^2.

2.3 Numerical Simulations

The experimental configuration was simulated in the finite element method based software COMSOL versions 5.5 and 5.6. The geometry used for the simulations, consisting of glass, Au film, and water, is shown in Fig 2.3. A port is included on the glass side from where a Gaussian laser beam is incident at an oblique angle. All quantities are plotted in the XZ and XY planes as depicted in the figure. The parameters used for the simulations in this work are listed in the Table 2.1.

2.3.1 Electric field

We use the electromagnetic wave, frequency domain (*ewfd*) physics module for computing the electric field distribution in such a configuration. Second-order scattering boundary conditions are applied to all boundaries except the ports. This is because, in *ewfd*, when light is not incident normally, there can be a significant reflection from other boundaries. Second-order treatment does not eliminate these effects but still functions better than first-order scattering boundary conditions. Ideally, one should use perfectly matching layers

Table 2.1: Parameters used in COMSOL simulations

Parameter	Notation	Value
Electric field magnitude	E_0	1 V/m
Waist radius	w_0	0.8 μm
Wavelength	λ	532 nm
Rayleigh range	x_0	$\pi w_0^2/\lambda$
Angle of incidence at glass-water interface	θ	40^o
Length of box	L_x	7 μm
Width of box	W_y	3 μm
Height of glass	H_g	2 μm
Height of water	H_g	1 μm
Thickness of Au	t	50 nm
Thermal conductivity of Au	κ	314 W/m.K
Density of Au	ρ	19300 kg/m^3
Heat capacity at constant pressure of Au	C_p	128 J/kg.K
Refractive index of silica glass	n_g	1.45
Refractive index of water	n_w	1.33
Relative permittivity of water	ε_r	n_w^2

(PML) to simulate such structures, but due to multiple ports and complex geometry, it is tricky to get a continuous PML domain around our geometry. Thus, the geometry dimensions are carefully chosen to minimise the effects due to reflections from the walls. The electric field expression to simulate a Gaussian intensity in the XY-plane, travelling along the Z-direction is given as [27]

$$\mathbf{E}^{\mathrm{G}}(\rho,z) = \mathbf{E}_0 \frac{w_0}{w(z)} e^{-\frac{\rho^2}{w(z)^2}} e^{+ik_{\mathrm{m}}z - i\zeta(z) + ik_{\mathrm{m}}\frac{\rho^2}{2R(z)}} \tag{2.1}$$

Where k_m is the wavenumber, $\rho = \sqrt{x^2+y^2}$ is the radial cylindrical coordinate, $z_0 = \pi w_0^2/\lambda$ is the Rayleigh range, $w(z)$ is the beam width,

$$w(z) = w_0\sqrt{1+\frac{z^2}{z_0^2}} \tag{2.2}$$

$R(z)$ is the wavefront radius,

$$R(z) = z\left(1+\frac{z_0^2}{z^2}\right) \tag{2.3}$$

and $\zeta(z)$ is the phase correction term,

$$\zeta(z) = \mathrm{atan}\left(\frac{z}{z_0}\right). \tag{2.4}$$

However, in our system, the Gaussian intensity does not travel in a standard z-direction. Instead, looking at the experimental configuration and trying to replicate it in the simulation geometry, the port will direct the light at an angle in the XZ-plane so that the electromagnetic wave hits the interface in the XY-plane. In such a configuration, the Gaussian beam simulated is

$$\mathbf{E_x}(x,y,z) = \mathbf{E}_0 cos\theta e^{-\frac{(x-x_0)^2+y^2+(z-z_0)^2}{w(z)^2}} e^{+i(kxsin\theta+kzcos\theta) - i\zeta(z) + ik_{\mathrm{m}}\frac{(x-x_0)^2+y^2+(z-z_0)^2}{2R(z)}} \tag{2.5}$$

$$\mathbf{E_z}(x,y,z) = -\mathbf{E}_0 sin\theta e^{-\frac{(x-x_0)^2+y^2+(z-z_0)^2}{w(z)^2}} e^{+i(kxsin\theta+kzcos\theta) - i\zeta(z) + ik_{\mathrm{m}}\frac{(x-x_0)^2+y^2+(z-z_0)^2}{2R(z)}} \tag{2.6}$$

Having only E_x and E_z components, this electromagnetic wave is polarised in the XZ plane, perpendicular to the direction of propagation and in the plane of incidence. Depending on the angle of incidence, we can get transmission into water or TIR into glass. However, since 50 nm thick Au film effectively acts like a mirror, we get TIR for all incidence angles, as shown in Fig 2.4 for incidence angles $40^o < \theta_c$ and $66^o > \theta_c$. Upon removing the Au film, we will retrieve the expected transmission for angles greater than critical angles, as shown in the right panel of Fig 2.4.

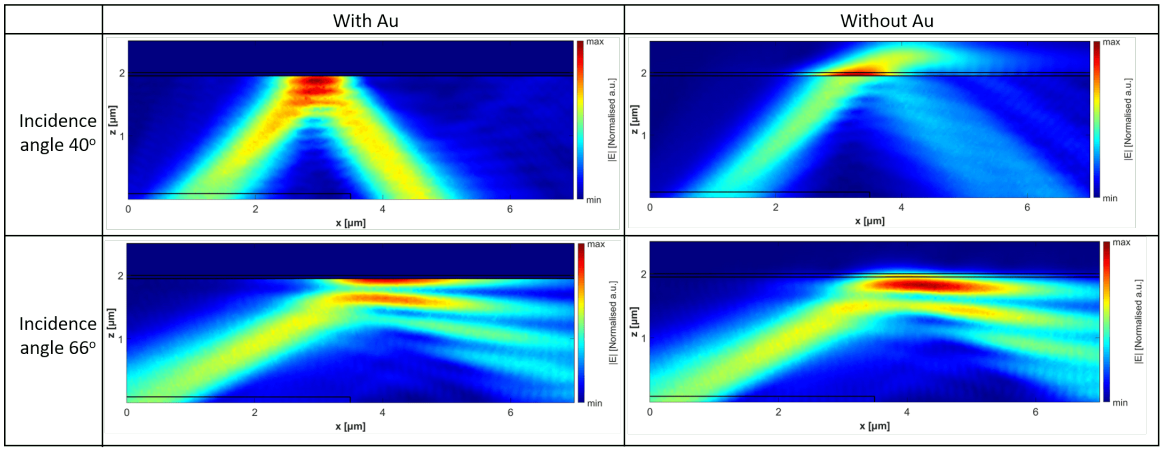

Figure 2.4: A Gaussian intensity electromagnetic wave is incident from the port such that it hits the glass-water interface at an angle $40^o < \theta_c$ (upper panel) and $66^o > \theta_c$ (lower panel). With Au coating (left) acting like a mirror, the light gets reflected back in both cases. But without Au coating (right), it transmits for an angle smaller than the critical angle and gets reflected for an angle greater than the critical angle.

2.3.2 Meshing

Meshing the domains is one of the critical steps in these simulations since it decides whether the field quantities can be resolved accurately at a small enough length scale. Physics-controlled meshing is not usually able to resolve the fields since the Au domain is much smaller compared to water or glass. By default, for *ewfd* frequency domain studies, the maximum mesh element is set to have a dimension of $\lambda/5$, which in our case will be ~ 106 nm. But, the thickness of the Au domain itself is 50 nm. Moreover, the mesh dimension should be such that it can resolve the decay/penetration of the field through the lossy media $\sim$ a few hundred nanometers. Thus, we resort to user-controlled mesh where each domain is meshed separately according to maximum and minimum mesh element sizes set by the user, as mentioned in Table 2.2. The domain with the finest mesh element size is meshed first, followed by the domains with increasing minimum mesh element sizes. This ensures that the mesh elements gradually merge in their sizes at the domain boundaries and the physical quantity is properly resolved. The resultant mesh formed is shown in Fig 2.5.

The *ewfd* module is solved using the frequency domain study, where the frequency is set to c/λ, since we are solving the model for a single frequency. Given the specifications of our workstation and the parameters of the problem, the model takes about 1.5-2.5 hrs time and 150-190 GB of memory to compute the electric fields. We then visualise the field near the Au surface in the water medium. The electric field appears meshy and grainy just at the Au-water interface. This is due to the meshing of the model, and a finer mesh would give

Table 2.2: User-controlled extremely fine mesh parameters

Domain	Maximum element size	Minimum element size
Au	40 nm	5 nm
Glass	80 nm	5 nm
Water	80 nm	5 nm

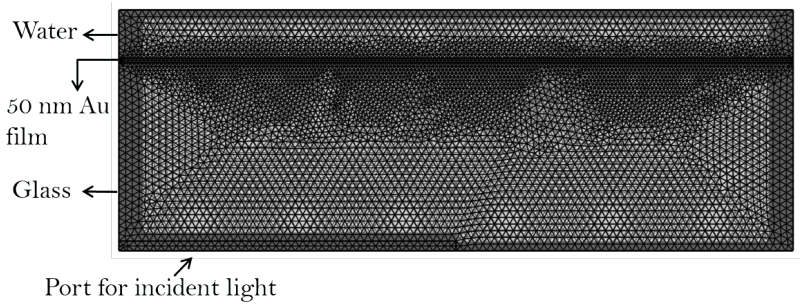

Figure 2.5: Meshed geometry for COMSOL simulations, showing the finest meshing of Au domain, followed by growing mesh boundaries for glass and water domains.

better results. However, we are limited here by the computational memory. Thus, instead, we look at the electric field in a plane 50 nm above the Au film, where the electric field appears relatively smoother, as will be shown in the following chapter. This is the surface plasmon excitation, which decays exponentially away from the surface.

2.3.3 Heat Transfer

Then, we add the heat transfer in solids and fluids (*ht*) module to the model. In the solids and liquids subnodes, select the solid and liquid domains appropriately. All properties are taken from the material library. Add a temperature subnode to specify the temperature of the outer boundary faces at room temperature (298 K). Add a heat source subnode and select the Au domain. Under the heat source settings node, select the general source and choose 'electromagnetic power loss density (ewfd/wee1)'. Now, under the multiphysics node, select electromagnetic heating. This will couple the *ewfd* and *ht* modules. Add a frequency-stationary study node and select the *ht* module as the physics to be solved for. Under the section 'Values of dependent variables', choose the user controlled setting for 'values of variables not solved for'. Select 'solution' under methods, 'frequency domain' under study and 'automatic' under parameter. This will ask the model to use the electric field values, solved by the previous frequency domain study, to compute the heating effect. Click on compute. With the available computational power, this simulation takes two to three minutes to finish. Under the results node, the 3D slice plot of the temperature will

depict the temperature distribution in the system due to the computed electric fields.

2.3.4 Fluid flow

To compute the fluid flow, add the laminar flow module (*spf*). In the physics model setting, select 'include gravity' and choose incompressible flow from the drop-down menu of compressibility. Under the fluid properties subnode, select temperature as computed by the *ht* module. Fluid properties like viscosity and density are to be taken directly from the material library. Subnodes of walls can be added to specify the condition for slip or no slip on the Au surface. In the gravity subnode, make g positive since our computational geometry is inverted. For the walls of the fluid column, set open boundary conditions. Then, under the multiphysics node, add 'nonisothermal flow' and select the 'Boussinesq approximation'. This is done to increase the convergence of the problem by assuming that the changes in density due to temperature rise are linear, that is, for small temperature rise. After this, add the stationery study step and select *ht* and *spf* physics to be solved. Under multiphysics coupling, select *nitf1*. Again, under 'Values of dependent variables', select user controlled settings for 'values of variables not solved for', 'solution' for method and 'frequency domain' for study. This will ask the model to solve *ht* and *spf* physics using solutions of *ewfd* physics. A 3D slice plot of fluid flow will be computed in the results node, and we can then extract the XY- and XZ-plane fluid flow profiles.

2.4 Brownian Dynamics Simulation in Matlab

A Brownian particle interacting with surface waves is bound to feel a optical forces, which can alter its Brownian dynamics. To study this, we simulate in Matlab the surface electromagnetic fields due to evanescent excitation on a glass-water interface.

We simulate the evanescent electric fields at a dense-rare interface, as indicated in Fig 2.6 in Matlab. Consider a plane monochromatic wave incident at an interface from medium 1 to medium 2 [33].

$$E_I(r,t) = E_{0_I} e^{i(k_I \cdot r - \omega t)} \tag{2.7}$$

$$B_I(r,t) = \frac{1}{v_1}(k_I \times E_I) \tag{2.8}$$

The reflected wave is then given as,

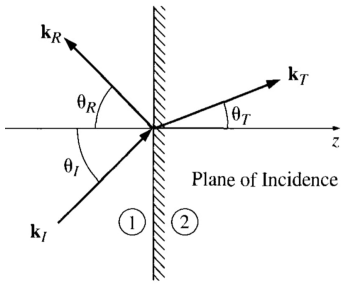

Figure 2.6: Ray diagram showing a plane wave with wave vector k_I incident from medium 1 on the interface with medium 2. The reflected plane wave has wave vector k_R and transmitted plane wave has wave vector k_T. θ_I,θ_R, θ_T are angles of incidence, reflection and refraction respectively [33].

$$E_R(r,t) = E_{0_R} e^{i(k_R \cdot r - \omega t)} \tag{2.9}$$

$$B_R(r,t) = \frac{1}{v_1}(k_R \times E_R) \tag{2.10}$$

and the transmitted wave is,

$$E_T(r,t) = E_{0_T} e^{i(k_T \cdot r - \omega t)} \tag{2.11}$$

$$B_T(r,t) = \frac{1}{v_2}(k_T \times E_T) \tag{2.12}$$

All waves have the same frequency ω, and the wave vectors are related as

$$k_I v_1 = k_R v_1 = k_T v_2 \tag{2.13}$$

From Fig 2.6 it can be deduced that for an obliquely travelling plane wave, the transmission wave vector can be expressed as,

$$\vec{k_T} = k_T(sin\theta_T \hat{x} + cos\theta_T \hat{z}). \tag{2.14}$$

The refractive indices of the two media are related to the wave velocity as $n_1/n_2 = v_2/v_1$.

2.4.1 Total internal reflection

At the critical angle θ_c, when $\theta_T = 90^o$, the transmitted wave grazes along the interface. From Snell's law we get

$$\begin{gathered} \frac{sin(90^o)}{sin\theta_I} = \frac{n_1}{n_2} \\ \frac{1}{sin\theta_c} = \frac{n_1}{n_2} \implies \theta_c = sin^{-1}\left(\frac{n_2}{n_1}\right) \end{gathered} \tag{2.15}$$

If $\theta_I > \theta_c$, then we get,

$$\frac{sin\theta_T}{sin\theta_I} = \frac{n_1}{n_2} \implies sin\theta_T = \frac{n_1}{n_2} sin\theta_I \tag{2.16}$$

If $n_1 > n_2 \implies sin\theta_T > 1$, we get,

$$cos\theta_T = \sqrt{1 - sin^2\theta_T} = i\sqrt{sin^2\theta_T - 1} \tag{2.17}$$

which is imaginary! This means there will be no transmitted wave. Substituting this into Eq 2.14, we can write $\vec{k_T} \cdot \vec{r}$ as:

$$\begin{aligned} \vec{k_T} \cdot \vec{r} &= k_T(sin\theta_T\hat{x} + cos\theta_T\hat{z}) \cdot (x\hat{x} + y\hat{y} + z\hat{z}) \\ \vec{k_T} \cdot \vec{r} &= k_T(xsin\theta_T + zcos\theta_T) \\ \vec{k_T} \cdot \vec{r} &= k_T(xsin\theta_T + iz\sqrt{sin^2\theta_T - 1}) \end{aligned} \tag{2.18}$$

This can be expressed in short as,

$$\vec{k_T} \cdot \vec{r} = kx + i\kappa z \tag{2.19}$$

Where,

$$k = k_T sin\theta_T = \frac{\omega n_2}{c} sin\theta_T \tag{2.20}$$

Using Eq 2.16, k can be expressed in terms of incident angle as,

$$k = \frac{\omega n_1}{c} sin\theta_I \tag{2.21}$$

And κ can be as (using Eq 2.16 again),

$$\kappa = k_T\sqrt{sin^2\theta_T - 1} = \frac{\omega}{c}\sqrt{n_1^2 sin^2\theta_I - n_2^2} \tag{2.22}$$

Using Eq 2.12 and 2.19, the total transmitted wave can be written as

$$E_T = E_{0_T} e^{i(kx + i\kappa z - \omega t)} = E_{0_T} e^{-\kappa z} e^{i(kx - \omega t)} \tag{2.23}$$

From the above equation, it can be understood that the amplitude has an exponentially decaying nature due to $e^{-\kappa z}$, perpendicular to the interface in the z-direction, while the wave propagates along the interface in the x-direction.

Incident p-polarised wave

Applying the boundary conditions for the continuity of electric and magnetic fields on either sides of the interface in the two media, we can derive the reflected and transmitted amplitudes of the electric fields:

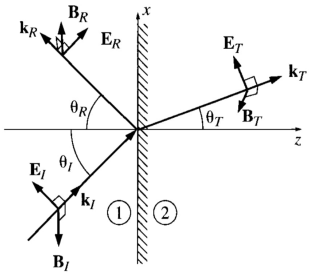

Figure 2.7: Ray diagram for p-polarised incident wave at the interface [33].

$$E_{0_R} = \left(\frac{\alpha - \beta}{\alpha + \beta}\right) E_{0_I} \tag{2.24}$$

$$E_{0_T} = \left(\frac{2}{\alpha + \beta}\right) E_{0_I} \tag{2.25}$$

Where

$$\alpha = \frac{cos\theta_T}{cos\theta_I} \tag{2.26}$$

$$\beta = \frac{\mu_1 v_1}{\mu_2 v_2} = \frac{\mu_1 n_1}{\mu_2 n_2} \tag{2.27}$$

The amplitude of the p-polarised transmitted wave can be written as,

$$E_{0_T} = E_{0_{T_x}} + E_{0_{T_z}} = cos\theta_T E_{0_T} \hat{x} - sin\theta_T E_{0_T} \hat{z} \tag{2.28}$$

Again substituting from Eq 2.16, 2.17, and 2.23 and simplifying in terms of θ_I, we get the resultant transmitted electric field as:

$$E_T = \frac{2cos\theta_I E_{0_I}}{n^2 cos\theta_I + i\sqrt{sin^2\theta_I - n^2}} e^{-\kappa z} e^{i(kx - \omega t)} (i\sqrt{sin^2\theta_I - n^2}\hat{x} - sin\theta_I \hat{z}) \tag{2.29}$$

Where $n = n_2/n_1$

Incident s-polarised light

Following the same protocol, the reflection and transmission coefficients can be obtained as

$$E_{0_R} = \left(\frac{2}{\alpha\beta + 1}\right) E_{0_I} \tag{2.30}$$

$$E_{0_T} = \left(\frac{1 - \alpha\beta}{1 + \alpha\beta}\right) E_{0_I} \tag{2.31}$$

Where α and β are given by Eq 2.26 and 2.27 respectively. The amplitude of the s-polarised transmitted wave having only a y-component can be written as

$$E_{0_T} = E_{0_{T_y}}\hat{y} \tag{2.32}$$

Going by similar substitutions as in the case of p-polarised case, the resultant transmitted electric field can be expressed as

$$E_T = \frac{2cos\theta_I E_{0_I}}{cos\theta_I + i\sqrt{sin^2\theta_I - n^2}} e^{-\kappa z} e^{i(kx-\omega t)}\hat{y} \tag{2.33}$$

2.4.2 Force calculation

We will use the dipolar approximation here, that is, consider the particle to be a very small dipolar sphere of radius $a << \lambda$. Then the optical force can be decomposed into gradient and scattering forces as described in the previous chapter,

$$F_{grad} = \frac{1}{4}\frac{Re\{\alpha_d\}}{c\varepsilon_0}\nabla I_i \tag{2.34}$$

$$F_{scat} = \frac{\sigma_{ext}}{c} S_i \tag{2.35}$$

The magnetic fields can be directly deduced from the electric fields as $B = (1/v)\cdot k \times E$ where v is wave velocity in the medium. Then, the poynting vector will be given by $S = (1/\mu_0)\cdot E \times B$. The complex polarisability of the dipolar particle is given by $\alpha_d = \alpha' + i\alpha''$ where the real and imaginary parts are [27]

$$\begin{aligned} \alpha' &= \frac{\alpha_{cm}}{1 + \frac{k^3\alpha_{cm}}{6\pi\varepsilon_0}} \\ \alpha'' &= \frac{\frac{\alpha_{cm}^2 k^3}{6\pi\varepsilon_0}}{1 + \frac{k^3\alpha_{cm}}{6\pi\varepsilon_0}} \end{aligned} \tag{2.36}$$

Where α_{cm} is the Clausius-Mossotti polarisability and k is the wave number of the incident light in vacuum. The forces obtained are then substituted into the overdamped Langevin equation to compute the Brownian dynamics of the particle.

$$\frac{dr}{dt} = \frac{-1}{\gamma}\frac{dU(r)}{dr} + \sqrt{2D}W(t) \tag{2.37}$$

Here, r is the position coordinate of the particle, $\gamma = 6\pi\eta a$ is the particle friction coefficient, $\sqrt{2D}W(t)$ is the white noise with intensity $2D$, D is the diffusion coefficient, W is a sequence of random numbers having zero mean and variance $1/\Delta t$, U is the external potential that the particle is subjected to and thus force $F(r) = -dU(r)/dr$ acts on the particle. Decomposing the equation into respective components [27],

$$\begin{aligned}
\frac{dx}{dt} &= -\frac{F_{grad_x}}{\gamma} - \frac{F_{scat_x}}{\gamma} + \sqrt{2D}W_x \\
\frac{dy}{dt} &= -\frac{F_{grad_y}}{\gamma} - \frac{F_{scat_y}}{\gamma} + \sqrt{2D}W_y \\
\frac{dz}{dt} &= -\frac{F_{grad_z}}{\gamma} - \frac{F_{scat_z}}{\gamma} + \sqrt{2D}W_z
\end{aligned} \tag{2.38}$$

Substituting the expressions for the respective forces, we can simulate the influence of evanescent fields on the Brownian dynamics of small dipolar particles.

Chapter 3

PLASMOFLUIDIC TRAPPING ASSISTED BY THERMOELECTRIC FORCES

Previously, in our group, a series of works has been performed aimed at harnessing the plasmonic field and mediated effects to manipulate colloidal matter on a large scale, as shown in Fig 3.1. For instance, surface plasmon polaritons are excited on a silver nanowire, and the resultant optothermal pulling can form a colloidal assembly [34] . A metal plate can replace the wire and be evanescently excited so that it serves as a heat source. This will again create an optothermal potential that can form a largescale 2D colloidal crystal [5]. Evanescent excitation can also be used to generate surface plasmons on a metal surface, which can be used to induce plasmon-mediated fluid flow and trap plasmonic nanoparticles on a largescale [6], which is otherwise challenging to do using optical tweezers .

In the above pieces of work, thermophoresis of the dielectric particles has been considered to understand the colloidal dynamics. That is, the colloids used exhibit negative thermophoresis [35], wherein they migrate from cold to hot regions . However, in the case of plasmonic particles that do not show thermophoresis, the dynamics have been attributed to the plasmonic fields and convective fluid flow. Recently, Franzl et al. [3] systematically investigated the significance of boundary layer fluid flows at the metal-water interface, which has considerable magnitude in the vicinity of plasmonic structures and can drive colloidal dynamics. This has not been included in the interpretation of the above-mentioned experimental results and it is the motive of this work to break down the contributions of the different forces at interplay in such plasmonic trapping systems. We start by investigating the silver nanowire system and the fields generated upon its excitation.

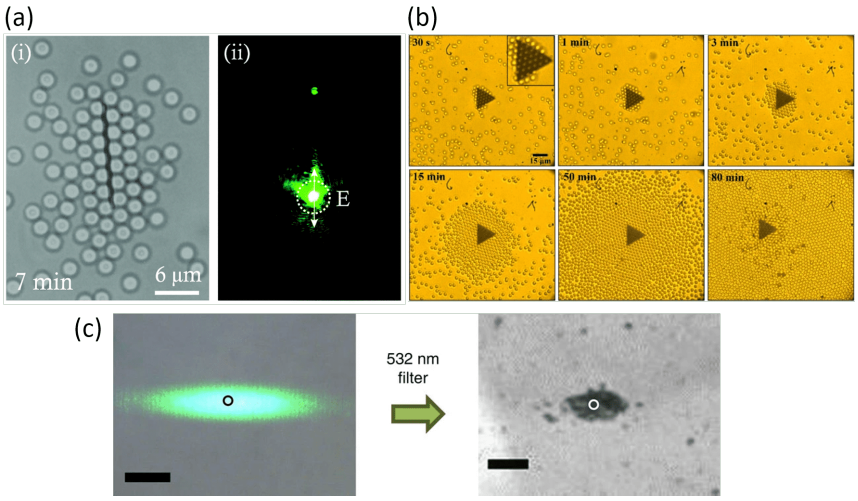

Figure 3.1: Surface plasmon assisted colloidal assembly. (a) A silver nanowire, anchored to a glass substrate, is illuminated by a 532 nm focused Gaussian laser beam on one end. Surface plasmon polaritons are excited and propagate along the wire, out-coupling at the other end as shown in (ii). The wire is placed in a water medium with 2 µm SiO_2 colloids dispersed, which form an assembly around the illuminated wire as shown in (i) [34]. (b) Au nanotriangle is anchored on a glass substrate and illuminated from the bottom using Kretschmann configuration. 2 µm SiO_2 colloids are dispersed in water which start to form a hexagonally packed assembly around the nanotriangle [5]. (c) Au film is illuminated using the Kretschmann configuration and as a result, Ag@Au core-shell particles accumulate at the excitation spot. The scale bar is 80 µm [6].

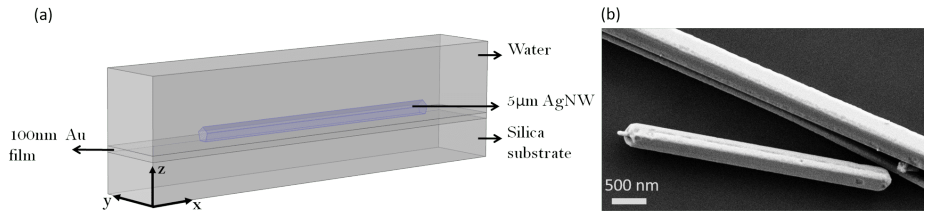

Figure 3.2: (a) Geometry used to simulate SPP on an AgNW, kept on an Au film-coated glass substrate in water medium. (b) SEM image of the chemically synthesized AgNW showing facets of the wire due to its pentagonal cross-section.

3.1 Simulating surface plasmon polariton and mediated fields

As depicted in Fig 3.1 (a), a stationary silver nanowire (AgNW) on a glass substrate is excited on one end by a focused 532 nm CW Gaussian laser beam. As a result, surface plasmon polaritons (SPP), which are resonant oscillations of the free electrons in the metal with incident electromagnetic wave [26], are generated and propagate along the AgNW surface, outcoupling on the other distal end. This can also be seen in Fig 3.1 (a)(ii). Around the wire, dielectric 2 μm SiO_2 colloids form an assembly as shown in Fig 3.1 (a)(i). We will simulate this system and try to understand the origin of this colloidal assembly.

We start by simulating the surface plasmons on the AgNW, as used in Fig 3.1(a), to estimate the extent of the role of plasmonic fields in colloidal dynamics. As described in the methods section, we construct a geometry wherein a silver nanowire of pentagonal cross-section is kept on an Au film-coated silica substrate in a water medium, see Fig 3.2(a). The pentagonal cross section is designed since experimentally the AgNW are chemically synthesized using the polyol process [36], which results in such a shape, also shown in Fig 3.2(b). The wire is modelled on top of an Au film so that the surface plasmons are effectively excited due to the incident and reflected laser beam, as shown in the scattered field plot of the electric field Fig 3.3. The geometrical parameters used are as mentioned in the Table 3.1.

3.1.1 Surface plasmon polariton electric field

To excite the surface plasmons, 900 nm Gaussian intensity light is incident from the port on one end of AgNW. The normalised scattered electric field is depicted in Fig 3.3, and the surface plasmons can be seen propagating along the wire surface, confined at the wire-water interface. The electric field was simulated for incident light of different wavelengths

Table 3.1: Parameters used in COMSOL simulations

Parameter	Notation	Value
Electric field magnitude	E_0	1 V/m
Waist radius	w_0	0.8 μm
Wavelength	λ	900 nm
Rayleigh range	x_0	$\pi w_0^2/\lambda$
Length of box	L_x	7.5 μm
Width of box	W_y	1.25 μm
Height of glass	H_g	2/3 μm
Height of water	H_g	4/3 μm
Thickness of Au	t	100 nm
Length of AgNW	l	5 μm
Length of each side of pentagon	d	150 nm
Thermal conductivity of Au	κ_g	310 W/m.K
Thermal conductivity of Ag	κ_s	419 W/m.K
Density of Au	ρ	19300 kg/m^3
Density of Ag	ρ	10800 kg/m^3
Heat capacity at constant pressure of Au	C_p	129 J/kg.K
Heat capacity at constant pressure of Ag	C_p	235 J/kg.K
Refractive index of silica glass	n_g	1.45
Refractive index of water	n_w	1.33
Relative permittivity of water	ε_r	n_w^2
Power of laser	P	10 mW

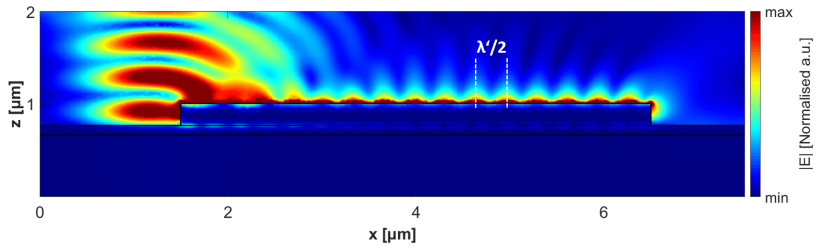

Figure 3.3: Normalised scattered electric field when one end of the AgNW is excited by a focused 900 nm Gaussian electromagnetic wave. The propagation of SPP can be seen along the wire-water interface, where λ' is the SPP wavelength.

and polarisations, and it was found that surface plasmons are most efficiently excited for an incident wavelength of 900 nm. This is related to the surface plasmon resonance condition and the length of the nanowire as well [37]. Such propagating surface plasmons, which are a result of coupled oscillations of the free electrons (plasma) of the metal to the applied electromagnetic field, are called surface plasmon polaritons (SPP). The dispersion relation of SPPs propagating at the interface of a metal with complex relative permittivity ε_m and dielectric with relative permittivity ε_d is given as [13]

$$k = k_0 \sqrt{\frac{\varepsilon_m \varepsilon_d}{\varepsilon_m + \varepsilon_d}} \tag{3.1}$$

Where k_0 is the wave vector of the incident electromagnetic wave in vacuum. Since $\varepsilon_m = \varepsilon'_m + i\varepsilon''_m$ is a complex quantity, the SPP wave vector is also complex, and the real part is written as

$$k' = k_0 \sqrt{\frac{\varepsilon'_m \varepsilon_d}{\varepsilon'_m + \varepsilon_d}} \tag{3.2}$$

For an incident 900 nm laser excitation, this can be used to calculate the wavelength of the propagating SPPs as

$$\lambda' = \lambda_0 \sqrt{\frac{\varepsilon'_m + \varepsilon_d}{\varepsilon'_m \varepsilon_d}} \tag{3.3}$$

Where λ_0 is the wavelength of incident light in vacuum. The relative permittivity of Ag at 900 nm is $-40.59 + i0.50969$, and that of water is $n_w^2 = 1.7689$. For $\lambda_0 = 900$ nm, this gives SPP wavelength ~ 662 nm, as is also indicated in the Fig 3.3.

Optical force due to SPP

Now, to calculate the optical force, an SiO_2 colloid with a diameter of 40 nm is scanned along the length of the nanowire, 8 nm above the AgNW surface. The small size of the

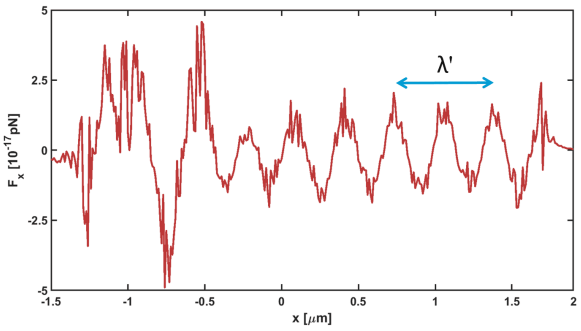

Figure 3.4: Optical force x-component on a SiO_2 colloid of diameter 40 nm simulated by integrating MST over the colloidal surface. Force is calculated at different positions along the wire, when the colloid is 8 nm above it, due to SPP field excited by a 900 nm Gaussian-profile electromagnetic wave.

particle is chosen so that its volume can effectively overlap with the SPP field and thus feel the plasmonic force. It is true that the calculated force will increase a little in case of a bigger particle, but it will still not affect the order of magnitude of the optical force, owing to the localised nature of the SPP field. The optical force is calculated by integrating the Maxwell stress tensor (MST) $\overleftrightarrow{T}$ over the surface of the spherical particle, for each position along the surface of the wire, at a height of 8 nm above it. The MST components can be written as [33],

$$T_{ij} \equiv \varepsilon_0 \left(E_i E_j - \frac{1}{2}\delta_{ij} E^2 \right) + \frac{1}{\mu_0} \left(B_i B_j - \frac{1}{2}\delta_{ij} B^2 \right) \tag{3.4}$$

where E_i, E_j, B_i, and B_j are the electric and magnetic field components respectively, δ_{ij}, called Kronecker delta, is 1 if $i = j$ and 0 otherwise, and μ_0 is the permittivity of vacuum. The MST component T_{ij} gives the force per unit area acting in the i^{th} direction on a surface having normal along j^{th} direction. To get the total force on a charge volume V, having surface area S and area element $d\mathbf{a}$, integrate the MST over the surface area as,

$$\mathbf{F} = \oint_{\mathscr{S}} \overleftrightarrow{\mathbf{T}} \cdot d\mathbf{a} \tag{3.5}$$

The resultant x component of the optical force, F_x, is shown in Fig 3.4. The magnitude of these forces, of the order of 10^{-17} pN, is extremely small to affect the dynamics of a nanoparticle or a microparticle. This indicates that optical forces alone are not sufficient to drive colloidal motion, like the formation of close-packed assemblies in Fig 3.1. Thus, in order to manipulate micro/nanocolloids effectively, plasmon-mediated effects like Joule heating of the metal and consequent fluid flow must play an important role.

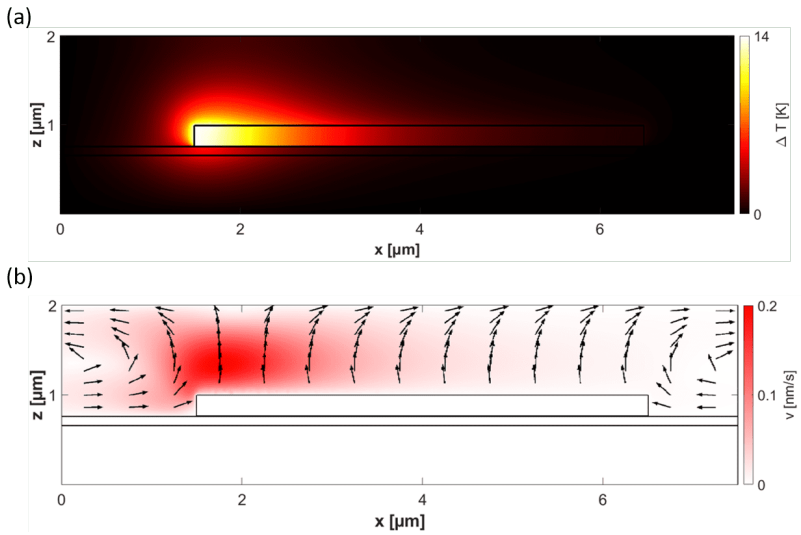

Figure 3.5: (a) The simulated temperature rise (relative to room temperature 298 K) in the AgNW and the surrounding water medium due to SPP excitation by a focused 900 nm Gaussian laser of power 10 mW. (b) Simulated convective fluid flow due to the temperature rise in (a).

3.1.2 SPP mediated temperature distribution and fluid flow

For this purpose, we utilise the electric field to compute the system's temperature distribution using the simulation method described in the previous chapter. The computed temperature profile in the XZ-plane cross-section is shown in Fig 3.5(a). The temperature decreases away from the excited end of AgNW, giving rise to a temperature gradient. Such temperature gradient will lead to fluid flow of two types: 1) convective fluid flow, which will arise due to temperature-dependent density fluctuations of the fluid, and 2) slip fluid flow, which is a boundary flow arising due to temperature gradient along the solid-liquid interface (detailed discussion in next section). Depending on the temperature gradient magnitude and the dimensions of the fluid column, either or both of the fluid flows can be significantly strong. We should keep in mind the possibility of viscous forces overpowering the optical forces and driving the colloidal dynamics.

Hence, the temperature simulation was followed by fluid flow simulation to compute the convective current in the system. But, since the height of the fluid column is extremely small, it is reasonable that convective flow will be very weak, and thus also the viscous force due to it. Also, in separate simulations [38], it has been observed that the convective flow velocity rises and saturates as the height of the fluid column increases without an increase in order of magnitude. The convective flow for the current geometry can be seen in Fig 3.5(b). In the case of slip flow, it is tricky to calculate the thermo-osmotic slip parameters

for the silver-water interface due to the complex geometry. But, as is shown by Franzl et al. [3], slip flow will significantly contribute to directing the colloid along the wire surface. Along with this, the thermo-osmotic flow along the particle's own surface will also lead to its thermophoretic motion. Since the particle is close to the plasmonic structure, it is not straightforward to distinguish between the effects of the thermophoresis of the particle and the slip flow along the wire. To understand the fluid flow mechanism and simplify the temperature distribution, it is imperative to move on to a simpler geometry where we can discuss more on these effects in greater detail.

3.2 Surface plasmons on a thin film: a simpler case

Another simpler geometry studied in our group can help us understand closely the role of slip fluid flow in plasmonic systems. This system studies the dynamics of plasmonic nanoparticles made of gold (AuNP) which do not show thermophoresis due to their high thermal conductivity. This will enable us to study the slip flow effects, excluding the colloid's thermophoresis. We will first study the system experimentally and then proceed to simulations.

3.2.1 Experimental results

Optical field

Consider a thin Au film coated on a glass/silica substrate. As described in the methods section, a solution of AuNP dispersed in water is prepared and drop-casted onto the film in a thin chamber geometry. The sample is kept on the prism in the Kretschmann configuration coupled to an upright microscope. The laser is allowed to enter the prism and undergoes TIR, generating evanescent waves which excite surface plasmons (SP) on the surface of the Au film. The SP field on the Au surface as viewed using a 4x, and 40x objective lens is shown in Fig 3.6. View from 40x lens (c) shows that the surface field has a speckle-like nature due to the roughness of the thermally evaporated Au film. Note that SPs are not excited at the resonance angle θ_{SPR}, due to which not all the incident power is coupled to the SP field.

As mentioned in the previous chapter, surface plasmons are effectively excited by p-polarised light, that is, an electromagnetic field having an electric field polarised in the plane of incidence. Using Maxwell's equations, it can be shown that s-polarised light cannot excite surface plasmons. Experimentally this can be seen in Fig 3.6, which shows a bright elliptical excitation for p-polarised light but very faint for s-polarised light. It is not perfectly

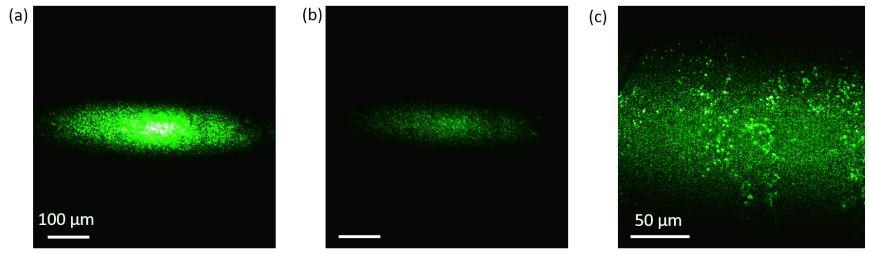

Figure 3.6: The evanescently excited elliptical spot on the Au surface, in water medium as viewed from the 4x objective lens in the (a) p-polarised and (b) s-polarised incident configuration. (c) Evanescent spot due to p-polarised incident laser viewed from the 40x objective lens.

dark for s-polarised light since the light may not be perfectly s-polarised, and the roughness of the Au film surface can contribute to further distortion of the polarisation.

Temperature rise

The evanescently excited optical field leads to heating of the Au film, whose temperature profile directly corresponds to the intensity profile in the homogenization regime, as was discussed in Chapter 1. That is, the Au film can be thought of as being composed of multiple nanoparticles placed very close to each other, such that collective effects occur when heated under laser illumination [29]. This gives a fully smooth temperature distribution around the excitation spot. Since the excitation spot does not have a spherical symmetry, it can be tricky to estimate the temperature experimentally. However, to get an order of magnitude estimate of the temperature rise, we used the phase transition of 5CB liquid crystal [38]. At room temperature, 5CB is in the anisotropic nematic phase. It undergoes a phase transition to isotropic phase when the temperature exceeds the phase transition temperature $T_{pt} = 35^o$ C. The boundary between the isotropic and nematic phases is clearly visible when viewed under a microscope due to the difference in refractive indices of the two phases. The change in the phase boundary size is linearly related to the change in incident power since $T \propto P$, and one can get an estimate of the maximum temperature rise at the heat source, which is the excitation spot in our case. This technique is commonly applied to determine the maximum surface temperature of a heated single particle since it leads to a circularly symmetric phase boundary, the radius of which can be directly calibrated with the power and, thus, the surface temperature of the particle.

For temperature estimation in our experiment, we sandwich a few microlitres of 5CB liquid crystal in a 10 µm thin chamber between a bare coverslip and an Au-coated coverslip. Fol-

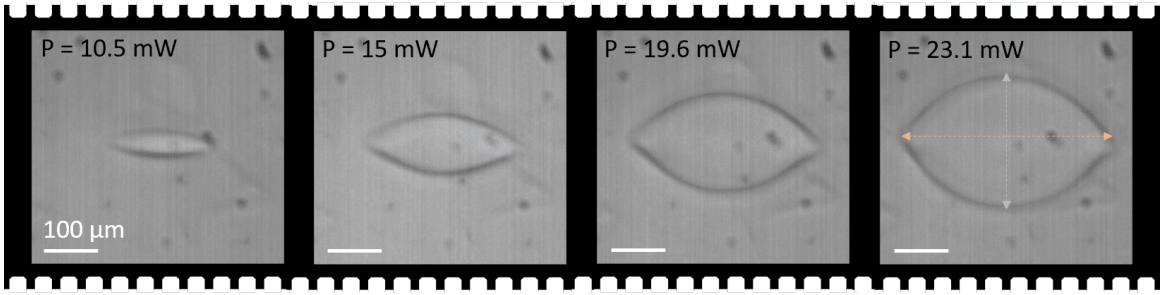

Figure 3.7: Temperature estimation using phase transition of 5CB liquid crystal. Upon illuminating the Au surface using TIR, the heat generated leads to a temperature rise. When $T > T_{pt}$, phase transition of 5CB from anisotropic nematic to isotropic phase takes place, the boundary of which is visible. Greater the temperature rise, larger is the phase boundary. The blue and orange double-headed arrows show the vertical and horizontal stretch of the phase boundary respectively.

lowing the same experimental protocol, the sample is placed under the microscope on the dove prism and excited using TIR. Multiple excitation spots will be visible in the camera due to the anisotropic nature of 5CB, but only one of those spots will lead to phase change. Since the excitation spot has an elliptic shape, it gives a pointy-elliptic phase boundary with no measure like a radius, as shown in Fig 3.7. As an approximation, we instead trace the change in the vertical and horizontal stretch of the boundary, which changes upon changing the excitation laser power, as can be seen in Fig 3.8. The vertical stretch of the boundary (blue dashed line in Fig 3.7) varies linearly with power till maximum experimental power is reached, whereas the horizontal stretch (orange dashed line in Fig 3.8) varies linearly only up to a certain power threshold $\sim$ 20 mW. This can be attempted to understand as follows: the excitation laser has a Gaussian intensity profile and falls obliquely on the interface. Due to such an incidence, the Gaussian intensity spot stretches asymmetrically more in one direction (horizontal in this case) than the other (vertical) direction. As the power rises, the central region of the excitation spot will always be more intense compared to the horizontal ends. Since the horizontal stretch does not show a linear rise, we fit the vertical stretch vs power variation with a linear equation, and do not consider the horizontal stretch. It is also to be noted that the temperature estimated using this approach gives a minimum bound to the surface temperature. As mentioned previously, multiple spots are visible in 5CB medium due to possible reflections within the anisotropic medium, which can lead to further distribution of laser power and underestimation of temperature. Also, in the actual experiment, metal nanoparticles contribute as well on top of the thermoplasmonic heat described here [29].

The temperature rise in 5CB medium can be estimated from the following expression [3]:

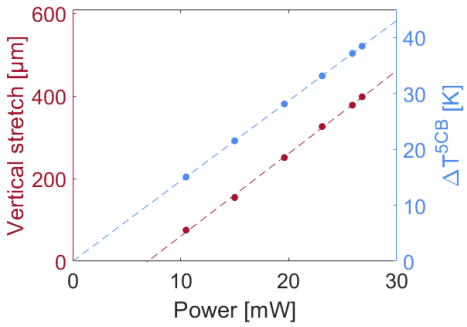

Figure 3.8: Temperature calibration using phase transition of 5CB liquid crystal. Vertical stretch of the phase boundary varies linearly with the incident power, as depicted by the red fit. Extracting the power at which phase transition begins, temperature rise in 5CB with respect to incident power can be plotted as shown by the blue fit.

$$\Delta T^{5\mathrm{CB}} = \frac{(35^{\circ}\mathrm{C} - T_0)}{P_{\mathrm{pt}}} P \tag{3.6}$$

Where T_0 is the room temperature, P is the incident power, and P_{pt} is the power at which phase transition begins. This means at P_{pt}, the vertical stretch will be just greater than zero. From the linear fit, $P_{pt} = 6.97$ mW. This gives $\Delta T^{5CB} \sim 1.43$ P. Since the thermal conductivity of water ($0.6\, Wm^{-1}K^{-1}$) is more than that of 5CB ($0.15\, Wm^{-1}K^{-1}$), the temperature rise in 5CB will be more than that in water. To get the corresponding temperature in water, $\Delta T^{H_2O} = 0.9 \times \Delta T^{5CB}$, which gives $\Delta T^{H_2O} = 1.29$ P. Fig 3.8 shows the variation of the vertical stretch and the temperature in 5CB with power. In our experiment, the maximum power used is 25 mW, which translates to a temperature of 57^o C in water. Considering that experimental approximation is an underestimate of the true experimental temperature, further simulations are carried out by optimising the simulated incident power such that a temperature rise of at least $\sim 50^o$ C is achieved.

3.2.2 Assembly of nanoparticles under plasmofluidic fields

Now that we have an idea about the temperature rise of the Au film due to TIR excitation, it will also dissipate heat into the sample solution in contact with the film. The sample solution contains AuNP of diameter 400 nm and the experiments are performed in a thin fluid film geometry as described in Chapter 2. It is observed that when sufficient laser power is incident, the AuNPs migrate towards the excitation spot and continue to accumulate as long as the power is supplied. This leads to a large-scale assembly of nanoparticles, as shown in Fig 3.9. As described in the previous section, optical forces in this configuration tend to be too weak to cause an assembly at such a large scale. We need to investigate the additional

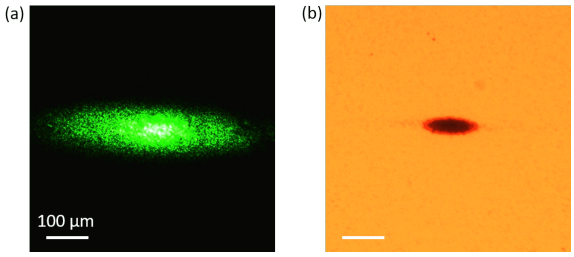

Figure 3.9: (a) Evanescently excited surface plasmon in the Kretschmann configuration, using a loosely focused, p-polarised 532 nm Gaussian laser beam of power 15 mW (before entering the prism), viewed from the 4x objective lens. (b) Assembly of plasmonic AuNP of diameter 400 nm formed upon plasmonic excitation as in (a).

effects of fluid flow, which can be classified into convective and slip fluid flows. These flows must play a role in driving the colloids to the excitation spot.

Convection arises due to temperature-dependent density fluctuations of the fluid medium. It will largely depend on the temperature variation normal to the heated surface. Whereas, slip flow arises due to gradients along the surface [39]. The interfacial interaction energy between a fluid and a surface can vary at different points on the surface due to different temperatures, concentrations, optical properties or an externally applied field [3]. In our experiment, we are concerned with temperature gradient-driven slip flow arising due to temperature gradient along the surface. Note that from previous simulations, it has been observed that convective flow velocities are very weak for thin fluid columns [38]. Thus, considering negligible convection, we will focus on the effects of slip fluid flow. But before that, we studied the effect of power and polarisation on the assembly formation.

AuNP assembly at high laser power

The initial experiment is carried out at a laser power of $\sim$ 50 mW and an elliptical excitation area spanning a length of upto $\sim$ 400 µm and breadth of $\sim$ 100 µm. The power and incident polarisation can be controlled using a combination of half-waveplates and polarisers. Fixing the power at 50 mW, we start with s-polarisation. Fig 3.10 shows the evanescent spot and AuNP assembly formed in this case. It is observed that the AuNPs accumulate at the centre of the excitation spot within a few minutes ($<$ 5 min), and a tightly packed assembly is formed. Now, the polarisation is changed from s to p, following which the AuNP start to disperse and form a loosely packed assembly, shown in Fig 3.10 below. A close up view of the AuNP assemblies for both polarisations viewed using 40x objective lens is also shown in the lower panel of the figure. At first glance, this seems counter-factual, as

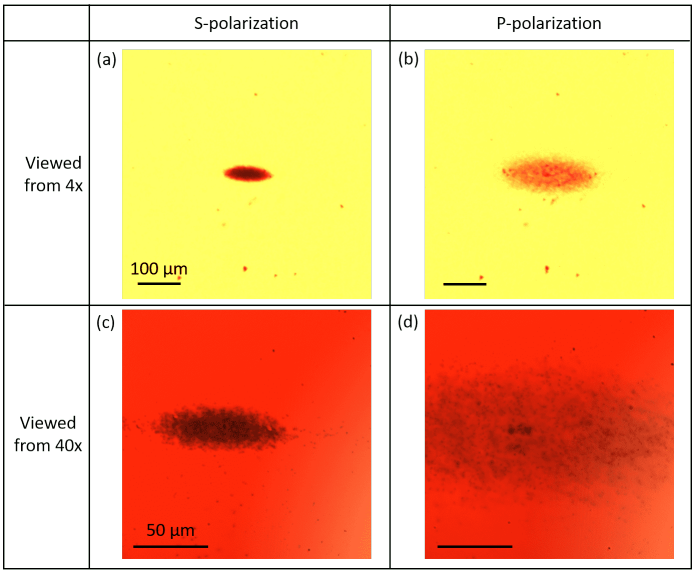

Figure 3.10: Assembly of AuNP (400 nm diameter) due to evanescently excited surface plasmons on an Au film using s- and p-polarized light of power $\sim$ 50 mW. The assemblies formed are visualised using a 4x and 40x objective lens.

previous conventional theory and experiments would suggest to expect the reverse: given the intensity of the optical field under s- and p-polarised incidence as shown in Fig 3.6, one would expect the p-polarised excitation to generate larger temperature rise and, thus greater fluid flow and a denser, tighter AuNP assembly. Whereas, due to faint excitation by s-polarised light, a smaller temperature rise is expected which should lead to a less dense AuNP assembly (ideally no assembly) due to the inability to excite surface plasmons [6].

Dielectric nanoparticles assembly at high laser power

To investigate the system and the role of surface plasmons further, we repeated the same experiment with 500 nm diameter SiO_2 dielectric nanoparticles (SiNP). We observe that the particles accumulate tightly for s-polarised incident light but form a vacant region in the centre and collect on the sides when p-polarised light is incident (see Fig 3.11). This observation is on the same lines as a similar experiment performed by [20] wherein 5 µm SiO_2 spheres were assembled on a 40 nm thin Au film using evanescently excited surface plasmons (1064 nm CW Gaussian excitation) in a thin 10 µm chamber. In their experiment, when the incident power was increased beyond a threshold, the colloids started to migrate away from the excitation spot and formed an elliptical ring, as shown in Fig 3.11(c). This effect is attributed to the thermophoretic nature of the colloids, which drives them away from the heat source [40]. The normal temperature gradients induce convection currents which push the colloids inwards towards the excitation centre. Whereas, the transverse tempera-

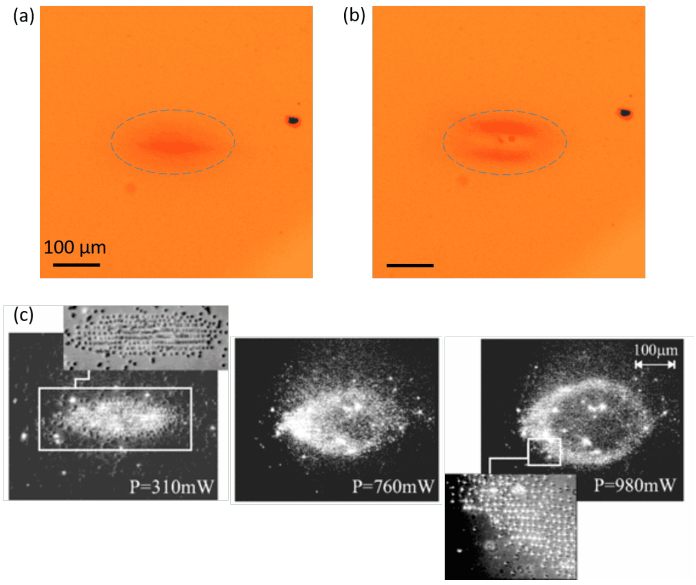

Figure 3.11: Assembly of SiNP having diameter 500 nm under (a) s-polarized and (b) p-polarized incident excitation, shown by gray-dashed boundary. Upon change of polarisation, the SiNP are seen to migrate away from the centre of the excited region forming a vacant elliptical region. (c) A similar experiment performed by [20] where 5 µm diameter SiO_2 colloids are assembled using a 1064 nm CW Gaussian laser in the Kretschmann configuration. The colloids are seen to form a vacant ring when power is increased.

ture gradient triggers the positive thermophoresis of colloids which forces them away from the excitation centre. While the thin chamber height limits the normal temperature gradient, the transverse gradients reduce farther away from the centre. At a distance from the excitation spot, the convective inward force is balanced by the outward thermophoretic force, allowing the particles to settle in an equilibrium state. This position of equilibrium can be controlled by changing the power, which directly affects the transverse gradients and, thus, the thermophoretic forces.

A similar mechanism of balance between thermophoretic and fluidic forces is at play here. P-polarised light excites surface plasmons very efficiently and thus leads to massive temperature gradients. The temperature gradients along the Au film surface lead to boundary layer fluid flows directed towards the excitation spot. The viscous forces push SiNPs inwards. Meanwhile, the thermophoretic nature of dielectric colloids also pushes SiNP inwards. However, beyond a temperature, the thermophoresis of the particles changes from thermophilic to thermophobic [41]. This is because of the sign change of the thermal diffusion coefficient D_T. Upon this transition, the colloids tend to migrate away from the excitation spot, leading to a vacant spot in the centre. At some distance, a balance between thermophoretic and fluidic forces is restored, causing the particles to form the two lobes

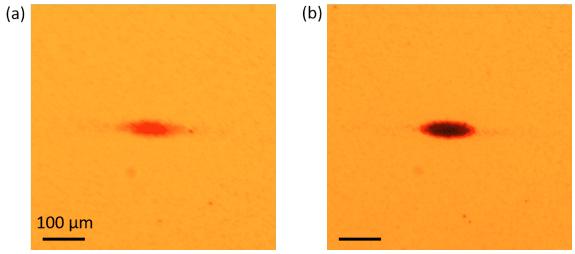

Figure 3.12: Assembly of AuNP due to evanescently excited surface plasmons on an Au film using (a) s- and (b) p-polarized light of incident power 15 mW. The assemblies formed are visualised using the 4x objective lens.

on the sides of the excitation spot. When we switch the polarisation from p to s, the effective temperature gradients are much smaller due to the lower intensity of surface plasmons. Here, the thermophoretic forces transit back to thermophilic nature and support the inward viscous forces, causing all the particles to assemble at the centre of the excitation spot. While this mechanism explains the assembly of dielectric particles, what about metallic particles that do not exhibit thermophoresis, like AuNP in our case?

AuNP assembly at low laser power

To understand this, we repeated the experiment but at lower laser powers. At an incident power of 15 mW, the observations align more with existing literature. P-polarised light produces a tightly packed AuNP assembly, whereas s-polarised light produces a loose assembly, as shown in Fig 3.12. No ring formation is observed like in the case of SiNP, but the tightly assembled particles in the centre become more diffused upon increasing the power, like in Fig 3.10(c). Now the question arises: why, upon increasing the power, does the AuNP assembly disperse? To understand this, we perform simulations to look at the forces at play in such a system.

3.2.3 Simulating surface plasmon mediated effects and forces

As described in the simulation methods section, we build the geometry to obtain evanescently excited surface plasmons on an Au film. Due to the computational expense of the system, we cannot simulate the geometry size having the experimental order of dimensions, which is a few hundred microns. Instead, we replicate in a smaller geometry of the order of a few microns, having a thinner fluid column. Also, the power of incident light is chosen such that the resultant temperature matches the experimental order of temperature rise. As

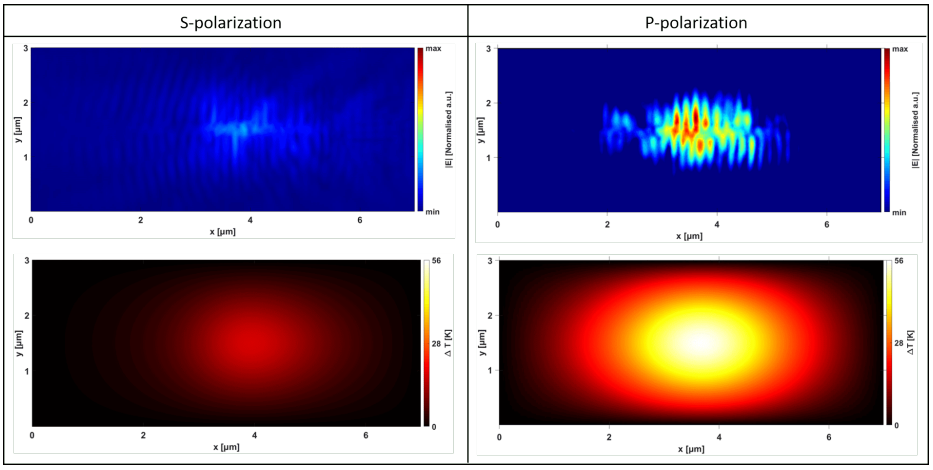

Figure 3.13: Electric field distribution (50 nm above Au film) and consequent temperature distribution (on Au film) generated using incident s- and p-polarised 532 nm Gaussian electromagnetic wave.

mentioned earlier, the height of the glass box is optimised so as to minimise the effect of reflections from the boundary walls. The studies are computed with appropriate meshing to simulate the electric field, temperature and fluid velocity distribution. The corresponding fields are shown in the figures in the methods section.

Since experiments were performed with s- and p-polarised light, we also did simulations for both polarisations. The top panel of Fig 3.13 shows a comparison between the electric fields excited on the surface in both cases, indicating that p-polarised light effectively gives surface plasmon fields. Thus, for force calculations, we will consider p-polarised incident excitation.

Optical forces

Coming to the forces at play, we first focus on the optical forces. We included a small sphere in the geometry and placed it above the excitation spot at a height such that its volume overlaps with the extent of the surface fields. Although our experimental AuNP of study has a diameter of 400 nm, for this simulation, we consider AuNP of diameter 100 nm placed 15 nm above the Au surface. This is because, due to computational costs, the height of the fluid column is very small and limited to 1 µm, and simulating a larger particle in this column requires much finer meshing. The x-coordinate of the particle is changed in steps of 25 nm from one end of the excitation region to the other, and the optical force is computed at each position. As mentioned before, for the wire geometry, this is done by integrating the Maxwell stress tensor (MST) over the particle surface. The resultant optical

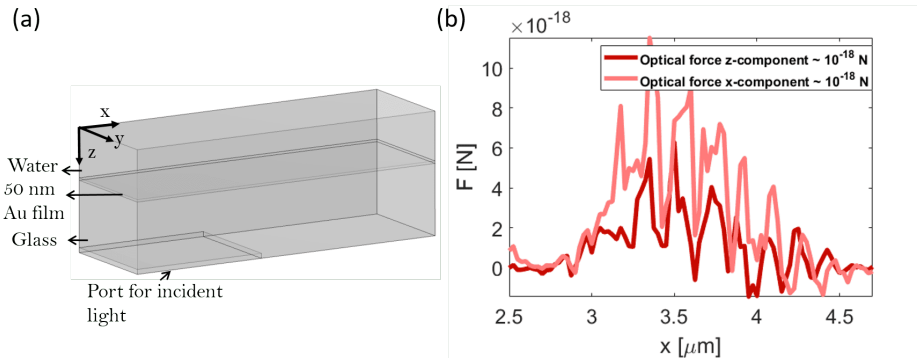

Figure 3.14: Optical force on a 100 nm diameter AuNP simulated in COMSOL, at different x-positions along the excitation spot. The x-component of the force is positive, which implies that the AuNP is pushed along the excitation spot. The z-component of the force is also positive, which, according to the coordinate system, means that the particle is pushed down onto the Au surface.

force components (x, y, and z) are obtained at each position. The x and z components are plotted as shown in the Fig 3.14(b). For reference, the coordinate system used in the geometry is shown alongside the optical force plot. A positive x-component means it pushes the particle along the propagation direction and thus acts like the scattering force. A positive z-component pulls the particle closer to the surface, acting like the gradient force. Meanwhile, the y-component is ~ 0 compared to the x- and z- components.

We should note here the order of magnitude of the optical forces, which is $\sim 10^{-18}$ N. This order of force is too small to manipulate the dynamics of a highly Brownian nanoparticle. Thus, optical forces alone cannot be responsible for the migration and assembly of AuNP. Note that the experimental particle is three times larger than the simulated particle (400 nm diameter). To estimate the forces on such a particle, we computed the optical force on a 400 nm AuNP when placed at the centre of the excitation spot, 10 nm above the Au film. The order of optical forces comes out to be 10^{-19} to 10^{-21} N. One would have expected the optical force to increase due to the larger volume of the particle. But it is even less than the 100 nm AuNP. This is because a larger ratio of the 100 nm AuNP volume interacts with the surface plasmon field and thus experiences greater force. Meanwhile, for the bigger 400 nm AuNP, a smaller proportion of its volume overlaps with the surface plasmon field, and therefore, the optical force exerted is smaller. From this, we conclude that the optical force is not strong enough to cause the largescale trapping/assembly of the AuNP at the excitation spot. We now need to look at optically mediated effects to understand the driving force behind particle accumulation.

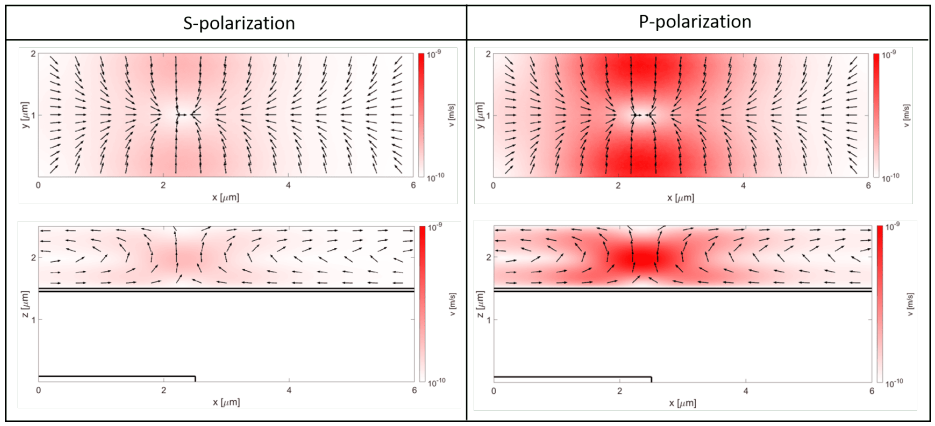

Figure 3.15: Convective fluid flow simulated using the temperature rise due to s- and p-polarized incident electromagnetic waves. Fluid flow profiles in the XY (50 nm above Au surface) and XZ ($y = 0$) planes are shown.

Optohermally-mediated fluid flow

One of the significant effects of illuminating a plasmonic material is the heat generated [29]. Upon excitation of surface plasmons, the Au film gets heated and leads to a temperature gradient in the normal and transverse directions. The corresponding temperature distributions for s- and p-polarisations are plotted in Fig 3.13, showing that s-polarisation leads to much less rise in temperature compared to the p-polarised case, which is obvious when considering the surface field magnitude.

The temperature gradients will naturally lead to fluid flow. As mentioned before, the temperature gradient along the surface will lead to slip fluid flow and that normal to the surface will lead to convective fluid flow. For computing the fluid flow, the height of the water box in the geometry is increased to 1 μm from 0.5 μm, and the length is reduced by 1 μm, to make it less computationally expensive. To simulate the convective fluid flow, the surface of the Au film is set to "no slip" boundary condition and all other settings are as described in the methods section. The simulation is coupled to the heat transfer module to obtain the fluid flow for temperature distributions under s- and p-polarised incident lights. The computed convective fluid flow profile is shown in the Fig 3.15 for s- and p-polarised excitations. Note the very small order of convective flow velocities at nm/s.

To simulate the slip fluid flow, the surface of the Au film is set to "slip velocity". We select the "thermal creep" option, and set the temperature to "Temperature (ht)", which will feed the temperature computed by the heat transfer module to calculate the fluid flow. For the thermal slip coefficient required by COMSOL, we use the value $\sigma_T = 0.001$ used by [3].

In their experiment, an Au film of similar thickness is heated using a focussed 532 nm Gaussian excitation. The trajectories of AuNP of diameter 250 nm are tracked to trace the fluid flow. The fluid velocity, approximated as that of the particle itself, is fitted with the equation:

$$v_{\parallel} = -\frac{1}{\eta}\int_0^{\infty} zh(z)\mathrm{d}z\frac{\nabla_{\parallel}T}{T} = \chi\frac{\nabla_{\parallel}T}{T} \tag{3.7}$$

Where χ, the thermo-osmotic coefficient, defines the fluid-solid interaction at the interface. Experimentally, they obtain $\chi = 10\times10^{-10}\ m^2/s$. Such a slip fluid flow in the liquid-solid boundary layer due to temperature gradient is called thermo-osmotic fluid flow. Two factors contribute to this:

1. The electric double layer (EDL) contribution arising from the electric double layer formed at the liquid-solid interface. It has a dependence on temperature gradients, permittivity gradients, salinity gradients and any external electric field applied. Considering only the temperature gradient in the system, the EDL contribution to the slip flow is

   $$v_{\parallel} = \frac{\varepsilon\zeta^2}{8\eta}\frac{1}{T}\frac{\mathrm{d}T}{\mathrm{d}x} \tag{3.8}$$

   Which gives χ as

   $$\chi_{\mathrm{E}} = \frac{\varepsilon\zeta^2}{8\eta} \tag{3.9}$$

   Where ε is the permittivity of water taken as $80\varepsilon_0$, and η is the viscosity of water. For AuNP, the zeta potential ζ used by [3] is -30 mV. In the citrate buffer, the AuNPs are stabilised due to a highly negative charge on their surface. The exact zeta potential to quantify this negative charge is estimated using electrophoretic light scattering. Substituting the values, this gives $\chi_E = 0.8\times10^{-10}\ m^2s$.

2. The Van der Waals contribution is a result of the potential energy of solvent molecules near a surface. The Hamakar constant A_H quantifies this interaction between two molecules across a medium [42]. Since A_H is larger for metals, [3] have used $A_H = 5\times10^{-20}$ J for a gold-water-gold system. The excess enthalpy due to Van der Waals' contribution is

   $$h_{\mathrm{vdW}}(z) = \frac{A_{\mathrm{H}}\beta T}{3\pi\eta z^3} \tag{3.10}$$

   This gives χ as

   $$\chi_{\mathrm{vdW}} = \frac{A_{\mathrm{H}}\beta T}{3\pi\eta d_0} \tag{3.11}$$

   Where $\beta = 0.2\times10^{-3}K^{-1}$ is the thermal expansion coefficient of water, and d_0 is the size of the solvent molecule, which for water is 0.2 nm. This gives $\chi_{VdW} = 9.3\times10^{-10}m^2/s$.

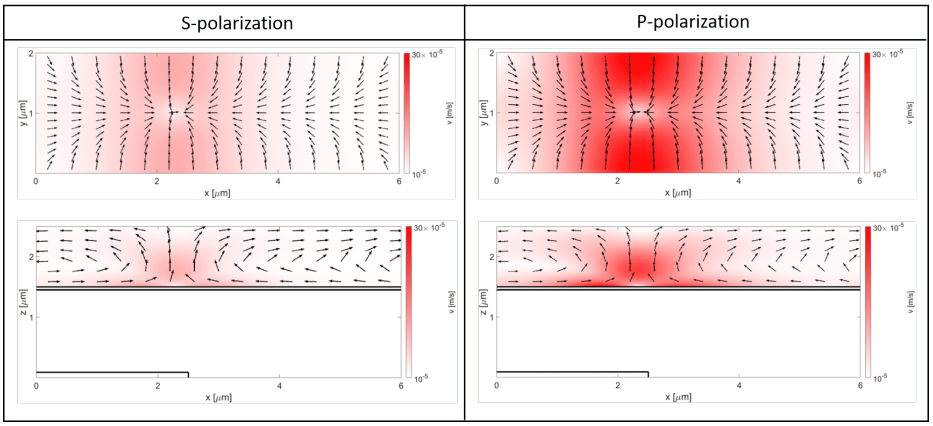

Figure 3.16: Slip fluid flow simulated using the temperature rise due to s- and p-polarized incident electromagnetic waves. Fluid flow profiles in the XY (50 nm above Au surface) and XZ ($y = 0$) planes are shown.

Upon adding the two contributions, it closely matches their experimentally obtained value of χ. Note that neither of the contributions depends on the exact temperature profile in the system. The Hamakar constant only depends on the materials and medium. The small zeta potential is a property of the particle and has little influence on the total value of χ. The resultant fluid flow profile depends on the temperature distribution, but not the thermo-osmotic coefficient, which depends only on the interfacial liquid-solid interactions. Thus, for our simulations, we have used the same value of χ for the gold-water-gold system. From χ, we can get the thermal slip coefficient using the relation

$$v_{\parallel} = \frac{\sigma_{\mathrm{T}} \eta}{\rho} \frac{\nabla_{\parallel} T}{T} \tag{3.12}$$

The first factor is χ. For water, $\eta = 0.001$ Pa s and density $\rho = 1000\ kgm^3$. Hence, χ is related to σ_T as

$$\sigma_{\mathrm{T}} = \chi \cdot 10^6\ \mathrm{m}^{-2}\ \mathrm{s} \tag{3.13}$$

Which, after substituting $\chi = 10 \times 10^{-10}\ m^2/s$, gives $\sigma_T = 0.001$. The resultant slip fluid flow obtained for s- and p-polarised light is shown in Fig 3.16. Note the order of slip flow velocities at μm/s, compared to nm/s in case of convective flow.

Fluidic forces

Clearly, the fluid flow due to p-polarised light is stronger than that due to s-polarised light. This is due to the temperature distribution generated by each of them. Thus, it should be emphasised that optical fields are contributing indirectly to the ”plasmofluidic” effects by mediating a temperature gradient, which induces fluid flow. Further simulations are

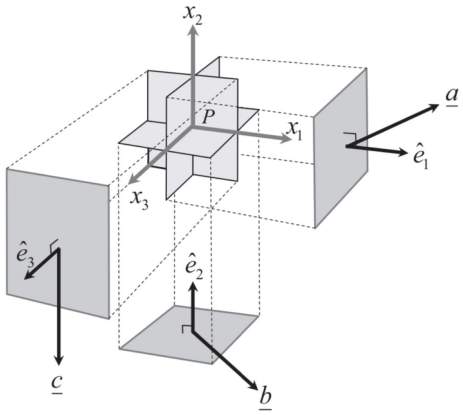

Figure 3.17: Fluid force exerted at a point P on a surface. x_1, x_2, x_3 are surfaces and $\hat{e}_1$, $\hat{e}_2$, and $\hat{e}_3$ are unit normal directions for the surfaces respectively [42].

therefore done for the p-polarised case. If a spherical particle is present in such a moving fluid, it will experience a force on its surface, specifically molecular stress on its surface in the moving fluid. This is given by a quantity called the viscous stress tensor, a 3×3 matrix, to calculate the magnitude and direction of molecular contact forces on a surface in a moving fluid [43]. The total stress tensor will contain all information about the stress at a point in a stationary/moving fluid. For a point P on an arbitrary surface, it is expressed as

$$\underline{\underline{\Pi}} = \begin{pmatrix} \tilde{\Pi}_{11} & \tilde{\Pi}_{12} & \tilde{\Pi}_{13} \\ \tilde{\Pi}_{21} & \tilde{\Pi}_{22} & \tilde{\Pi}_{23} \\ \tilde{\Pi}_{31} & \tilde{\Pi}_{32} & \tilde{\Pi}_{33} \end{pmatrix} \tag{3.14}$$

Where Π_{mn}, a function of fluid velocity, gives the stress at point P on the surface-m (x_m) in the direction-n (e_n), where $m,n = 1,2,3$, as shown in Fig 3.17. For a finite surface S, the total molecular fluid force is given by integrating the stress tensor over the surface of interest:

$$\underline{\mathscr{F}} = \iint_{\mathscr{S}} [\hat{n} \cdot \underline{\underline{\tilde{\Pi}}}]_{\text{at surface}} \, dS \tag{3.15}$$

Where n is the unit vector normal to the surface, and dS is the differential surface element. The stress tensor has contributions from viscous stress and pressure. The pressure force arises due to the difference in pressure across a surface, whereas the viscous force arises due to friction against the surface and acts opposite to the direction of flow. Considering the fluid to be incompressible, the pressure force can be ignored. If we calculate the viscous force which acts along the direction of friction and will be opposite to the fluid flow, then upon negating it, we can estimate the net fluid force that a nanoparticle will be subjected to [44]. For this purpose, in the simulation we added a "surface integration" under the "derived values" subnode of Results. We select the surface over which the force is to

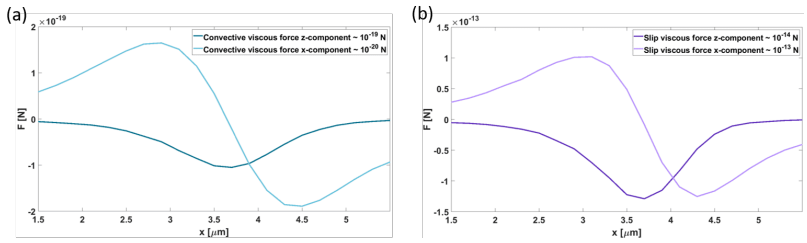

Figure 3.18: Convective and slip viscous forces on a 100 nm diameter AuNP at different x-positions above the Au surface. The fluid flow is simulated using the temperature profile computed from the p-polarised electric field (Fig 3.13). x- and z-components of the (a) convective and (b) slip viscous forces are shown.

be calculated, that is, the spherical particle. Under the expressions setting, select viscous stress in x, y, z directions, add a minus sign in front of each expression and then "Evaluate". This will give the negative viscous force exerted on the particle surface due to the simulated fluid flows. Since it is negative, it is actually indicating the direction in which the particle tends to move under the effect of the flow (opposite to friction force). Like for the optical force, the particle's x-position is changed from one end to the other in steps of 50 nm and negative viscous force is calculated at each position. The resultant x and z-components of the forces in the case of slip and convective fluid flows (induced by p-polarised incident light) are depicted in the Fig 3.18.

Consider the coordinate system shown in Fig 3.14 The x (and y) components of the viscous force act in the surface plane and push the AuNP towards the excitation spot. Whereas the z-component of the viscous force, being negative, acts vertically upwards, driving the colloids out of the excitation spot. We should note the difference between the order of magnitude of viscous forces due to convective and slip fluid flows. The convective viscous forces at 10^{-18} N are very weak to significantly affect AuNP dynamics. On the contrary, the slip viscous forces at sub-pN order are strong enough to move around the AuNP. We can get a tightly or loosely packed assembly of nanoparticles based on the relative strength of the in-plane (x and y) force components compared to the out-of-plane (z) force component. The particles remain tightly assembled as long as the in-plane forces dominate. As we increase the temperature, the out-of-plane forces can start to take over, forcing the particles upwards out of the trap.

Role of fluid column height

The fluid column height in our simulation (1 μm) is very thin compared to the experimental geometry (10 μm). The simulation needed to be run for a larger geometry to include the effects due to fluid column height. But, with the *ewfd* module, this is computationally too expensive for our system of study. From the force analysis, it is indicative that the optical forces have a negligible role to play. The major player is the viscous force, which is driven by the temperature gradient. If we can somehow replicate the temperature distribution without using the *ewfd* module, then the simulation with a large fluid column can be executed.

For this purpose, we use a tool called "Deposited beam power" in the heat transfer module. Under the *ht* node, keeping everything else the same, replace the "heat source" subnode with "Deposited beam power". Select the Au surface towards the water side in the boundary selection. Under beam orientation, we need to indicate the direction in which the beam is incident. Enter "-sin(θ)" in the x-component and "-cos(θ)" in the z-component. Under the settings of the beam profile, select built-in beam profiles, enter power $P_0 = 3.8$ mW, and appropriately choose the beam origin point. Select the distribution type as Gaussian and the standard deviation as 150 nm. The parameters have been carefully chosen such that a total temperature rise of ~ 50 K is achieved, to match the experimental order. Here, the simulation will take place assuming that a Gaussian laser beam of the mentioned power and standard deviation is incident on the selected boundary at the indicated orientation. The heat deposited by such a source under this configuration will result in the temperature rise of the Au surface, as shown in Fig 3.19. This temperature profile is a close approximation to the one obtained by coupling *ht* to *ewfd*, as shown in the Fig 3.13 for p-polarised case. Eliminating *ewfd* significantly lowers the required computational memory and time.

Now, we can easily crank up the dimension of the geometry and simulate the fluid flow in larger volumes. The slip fluid flow simulations were carried out for fluid columns of heights 1 μm, 21 μm, 41 μm, 61 μm, and 81 μm. The length and breadth of the geometry were increased to 10 μm each, from 6 μm and 2 μm, respectively. From Fig 3.19, it can be seen that the slip flow velocity magnitudes remain of the same order of magnitude. In fact, the presence or absence of the AuNP also does not affect the slip flow velocity. It has been shown previously that the convective fluid flow magnitudes increase only slightly upon increasing height and then remain nearly constant [38]. For our system, the convective flow rises to ~ 49 nm/s in an 81 μm high fluid column from 0.1 nm/s in a 1 μm high fluid column.

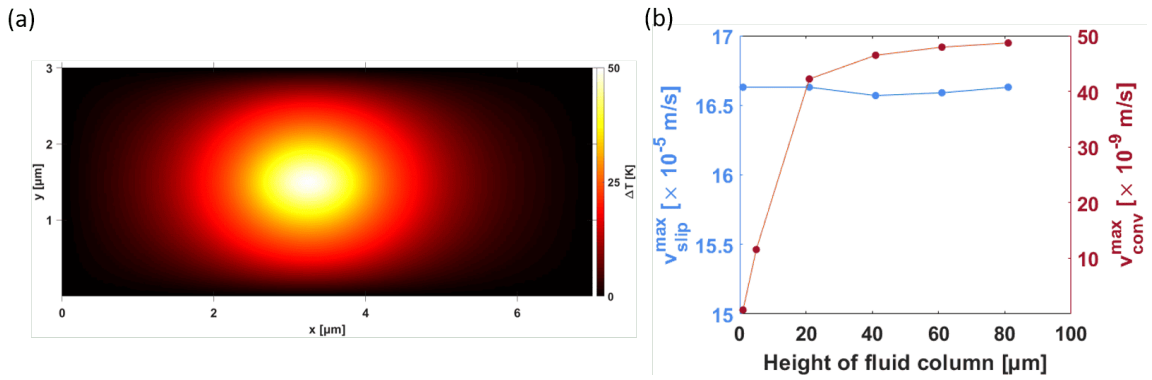

Figure 3.19: (a) The temperature distribution in the XY plane above the Au surface simulated using "Deposited beam power" method. (b) Variation of simulated maximum slip and convective fluid flows due to temperature profiles generated using (a).

Fluid flow and viscous forces in bigger geometry

Equipped with this information, for further analysis, the fluid flow is simulated in a fluid column of fixed height 4 µm, length 7 µm and width 3 µm. The slip and convective fluid flows in the XY and XZ planes are shown in the Fig 3.20. As can be seen, the convective fluid flow is stronger in the bulk, whereas the slip fluid flow is stronger near the surface. Moreover, the convective flow velocity is much weaker than the slip flow velocity, by three orders of magnitude. To quantify the effects of these flows on AuNP, we included in the simulation, a spherical AuNP at a height of 20 nm above the Au surface. Then, viscous forces are calculated on AuNP of diameters 400 nm, 250 nm and 150 nm under the conditions of slip and convective fluid flow. The x-position of the particle is changed from one end of the fluid column to the other, and the resultant x and z components of the forces are plotted, as shown in Fig 3.21.

Observe the difference between the slip and convective viscous force magnitudes again, indicating the negligible contribution of convective viscous forces. Also, as the size of the particle increases, the force profile becomes steeper, indicating a tighter trap. Experimentally also, this can be reaffirmed by the fact that smaller particles are confined loosely and over a larger area compared to bigger particles, as shown in Fig 3.22. The experimental protocol remains the same except that now 250 nm and 150 nm diameter AuNPs are used. Here on, we will refer to the F_y and F_x forces as in-plane forces since they act in the plane of the excitation spot, and F_z as out-of-plane force since it acts perpendicular to the excitation spot. Thus, from Fig 3.21 the out-of-plane viscous force (F_z) is stronger than the in-plane force (F_x) in the centre of the excitation spot. This means that once the particle crosses over to the central part, the out-of-plane forces will push it upwards away from the surface (refer

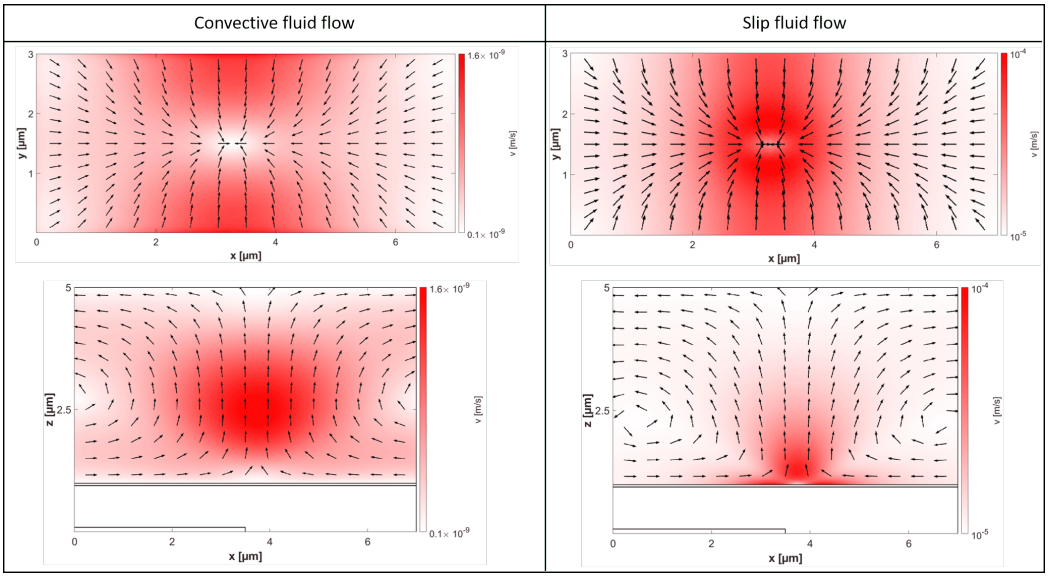

Figure 3.20: Convective and slip fluid flows simulated in a larger fluid box using temperature distribution as computed using Deposited beam power. The fluid flow profiles in the XY and XZ planes are shown.

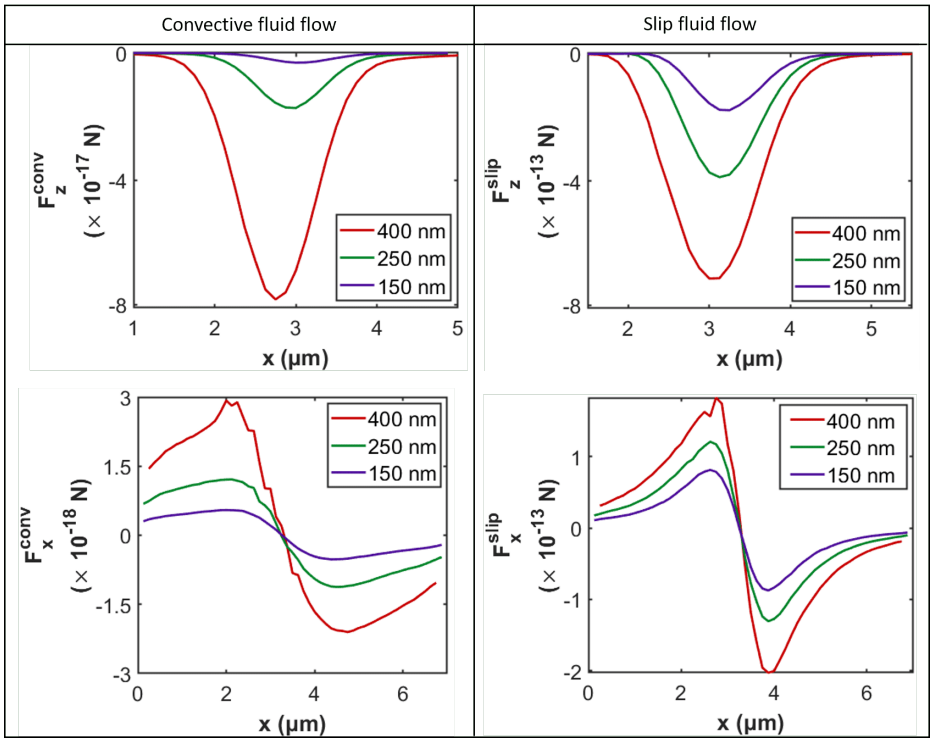

Figure 3.21: Slip and convective viscous forces exerted on AuNP of diameter 150 nm, 250 nm, 400 nm. The x-component (in-plane) and z-component (out-of-plane) forces are plotted.

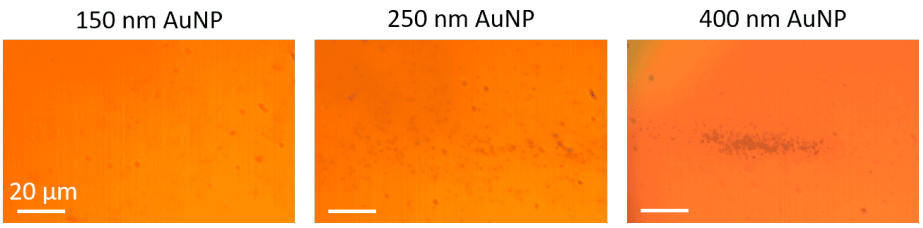

Figure 3.22: Accumulation of AuNP under p-polarised evanescent excitation of incident power 19.5 mW, visualised from the 40x objective lens. AuNPs of diameter 150 nm do not accumulate and are visible as very faint dots. AuNPs of 250 nm diameter accumulate over a very large area. Whereas, AuNPs of diameter 400 nm accumulate in a smaller space.

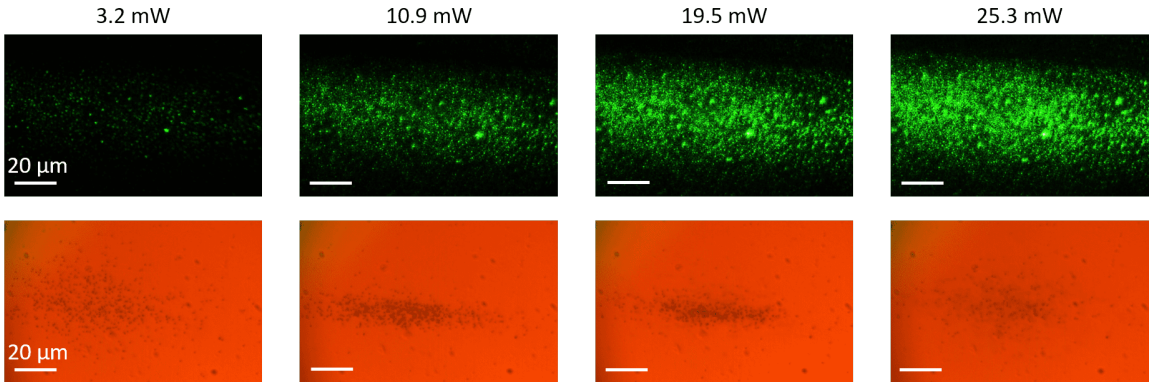

Figure 3.23: Power dependent assembly formation of 400 nm diameter AuNP visualised from the 40x objective lens. The top panel shows the evanescent excitation spot and bottom panel shows the consequent assembly of AuNPs.

to the coordinate system in Fig 3.14). When the particle is beyond the central region, again, in-plane forces will guide it towards the centre. Experimentally, such particle dynamics are clearly observed, wherein the AuNP can be traced approaching the excitation spot and then diffusing out of focus as it comes closer to the centre [39]. At lower powers, a net particle density is maintained in the centre despite such approaching and diffusing. But as the power increases, the AuNP diffuse out of focus even when farther from the centre, due to much stronger out-of-plane forces. This prevents them from being closely packed, like at lower powers. An experimental series of the AuNP accumulation with rising powers (and thus temperature) is shown in Fig 3.23. As the power increases, the temperature rises, and (slip) fluid flows become stronger. The colloids are driven to the excitation spot and packed tighter with rising power. This depicts the strengthening of the in-plane fluid flows. But, at high enough power, the out-of-plane fluid flows become stronger than in-plane flows, forcing the colloids out of the excitation spot and thus lead to the formation of a dispersed assembly.

The simulations and experiments indicate that surface plasmon-mediated optical forces are too weak to hold the particles in the excitation region. The fluidic forces drive the particles towards the excitation region, where, again, the convective forces have a negligible contribution, and the slip fluid flow supplies the major force. Comparing the magnitude of viscous and optical forces, it is clear that particles accumulate due to the (slip) fluid flow, and the optical forces are too weak to hold the particles in the excitation region. The major contribution of the plasmonic field here is to facilitate the temperature rise, which induces the fluid flow. On the same note, changing the polarization only affects the surface plasmon generation, which in turn directly affects the rise in temperature, consequently altering the fluid flow. From this analysis, it is conclusive to say that slip-fluid flow is the main driving agent for such large-scale nanoparticle manipulation, which is mediated by temperature rise in this case.

3.2.4 Pattern formation under plasmofluidic effects

Using this information, we also tried to explain the formation of patterns of nanoparticles when under multiple plasmonic excitation spots, as shown in Fig 3.24 [7]. In a very similar experimental geometry, multiple evanescently excited spots are created. The sample solution contains Ag@Au core-shell nanoparticles, which form the patterns shown under such multiple excitations. Here, we attempt to explain such pattern formation by trying to infer the forces exerted by the complex fluid flow. This will be in contrast to the explanation provided by the authors, crediting the pattern formation to plasmonic field interference.

As shown in Fig 3.25 and 3.27, we tried to simulate the rise in temperature and fluid flow for such dual and quadruple illuminations (Fluid column dimensions for dual excitation simulations: length 8 μm, width 2 μm, height 1 μm; quadruple excitation simulations: length 8 μm, width 5 μm, height 1 μm). Multiple hotspots result in a complex fluid flow showing unstable equilibrium positions (points of zero velocity). Looking at the dual excitation case in Fig 3.26, for the slip fluid flow profile 50 nm above the Au surface, the centre between the two hotspots is also a point of minimum velocity where in the y-direction, fluid velocities approach the same point, but in the x-direction, the fluid velocities diverge away. Similarly, for the quadruple excitation case in Fig 3.28, in the centre of the 4 excitation spots, there is a similar minimum in fluid velocity but with approaching flows along y-direction and diverging flows along x-direction. From experimental images, it is observed that particle accumulation happens at exactly such positions. However, given the directions of fluid flows, it is unclear how the assembled particles are stable in these positions.

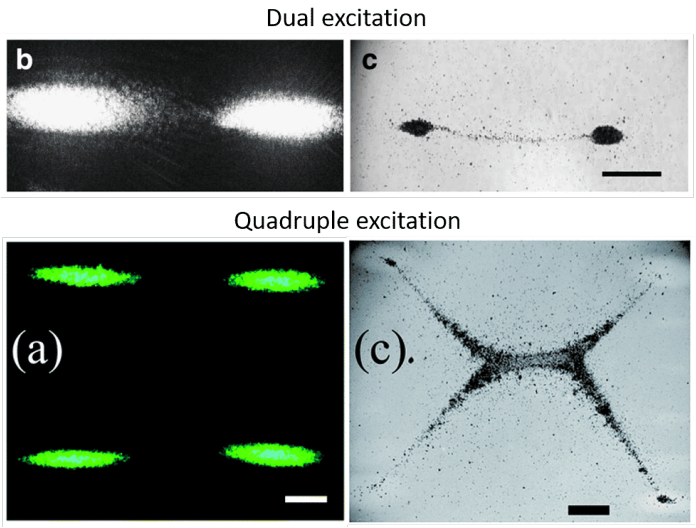

Figure 3.24: Pattern formation under multiple excitations. The nanoparticles used are Ag@Au coreshell particles (Ag-core-Au-shell) (scale bar = 200 µm) [7]

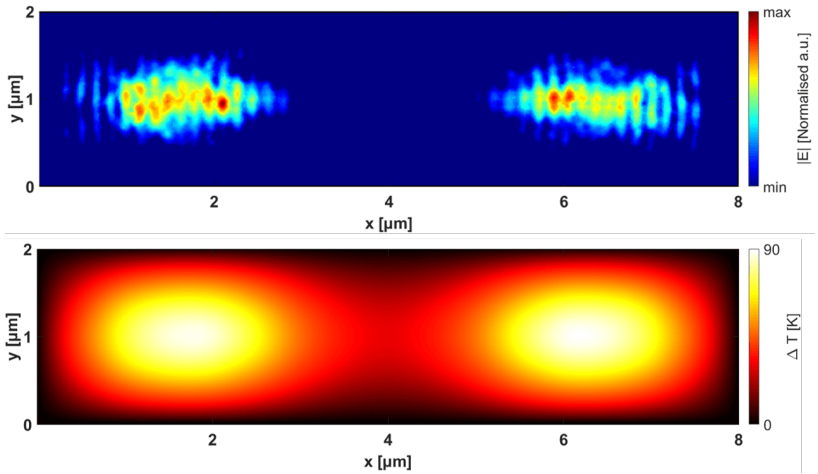

Figure 3.25: Electric field (50 nm above Au surface) and temperature distribution (of Au surface) in the XY-plane obtained by simulating two oblique incidence Gaussian beams.

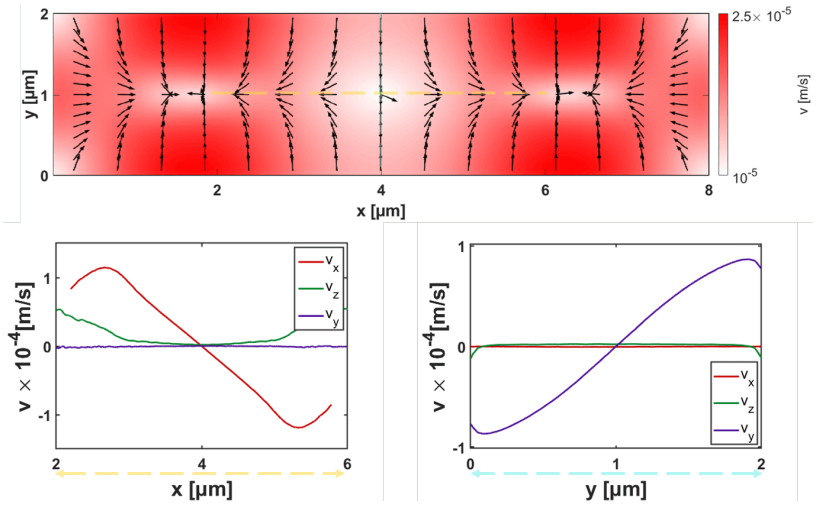

Figure 3.26: Slip fluid flow profile generated due to temperature distribution as obtained in Fig 3.25. The bottom panel shows the fluid velocity components along the yellow (X-axis) and blue (Y-axis) dashed lines in the fluid flow profile.

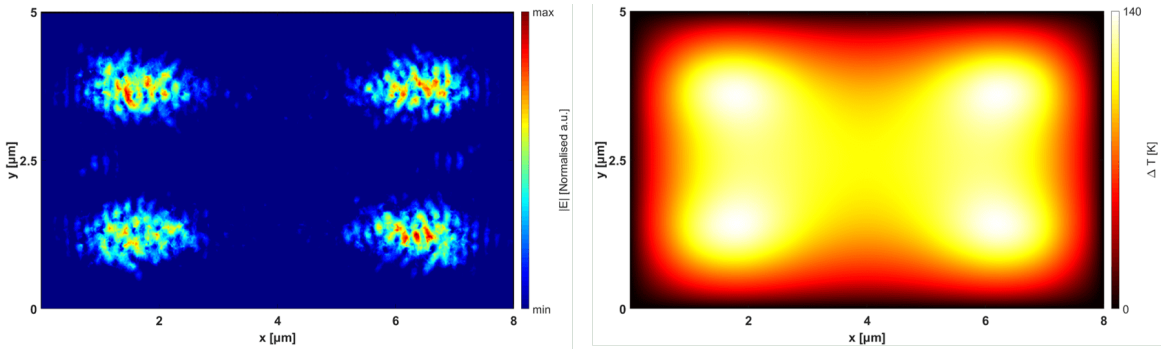

Figure 3.27: Electric field (50 nm above Au surface) and temperature distribution (of Au surface) in the XY-plane obtained by simulating four oblique incidence Gaussian beams.

Clearly, it is an effect of complex fluid flow near the Au surface and not the interference of surface plasmon fields as predicted in the published work, since the optical forces are too weak. A line profile of the fluid velocity components $(-v_x, -v_y, -v_z)$ for a line passing through the centres of the XY-plane ($x = 4$ µm and $y = 1$ µm) is shown in Fig 3.26. The negative components are plotted to correspond directly with the force acting on a particle in a moving fluid. This will give a prediction of the direction of the viscous force that will drive the particle in x, y, and z directions. For the dual excitation, looking at the v_x plot along the X axis (left plot in Fig 3.26), a stable equilibrium can be expected in the centre of the two excitations. Comparatively, v_y and v_z are weaker. Also, v_z is always positive, indicating the upward pull on the particle, which is minimum in the centre of the two excitations spots (at $x = 4$ µm).

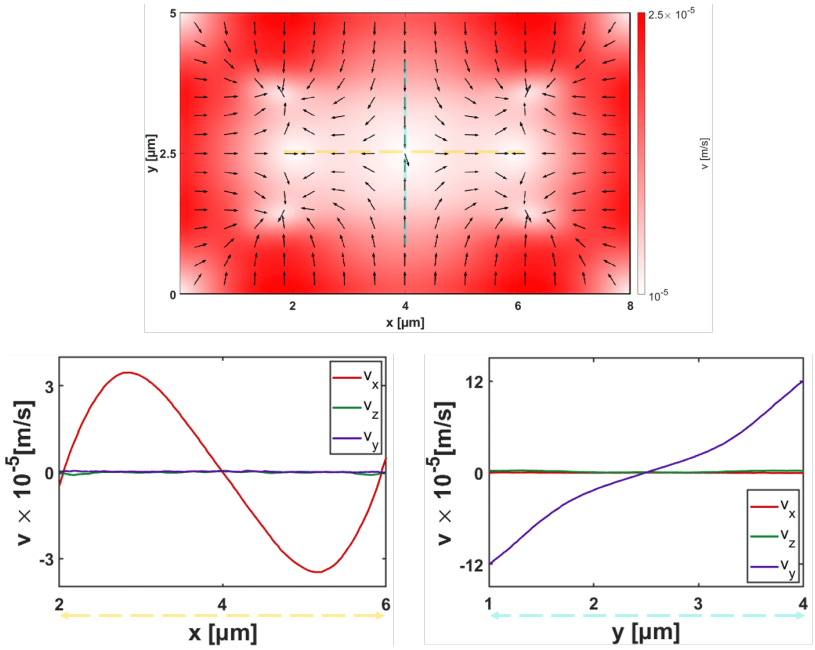

Figure 3.28: Slip fluid flow profile generated due to temperature distribution as obtained in Fig 3.27. The bottom panel shows the fluid velocity components along the yellow (X-axis) and blue (Y-axis) dashed lines in the fluid flow profile.

For the quadruple excitation, the corresponding electric field and temperature distributions are shown in Fig 3.27. The resultant slip fluid flow generated due to the temperature distribution is shown in Fig 3.28. Plotting v_x along X axis again (left plot in Fig 3.28), three equilibrium positions are expected along the X-direction, out of which the centre one (at $x = 4$ µm) is the stable equilibrium. This gives a possible explanation for the particles assembling in the common centre of the quadruple excitations. Again, v_y and v_z are much weaker compared to v_x component. Plotting v_x, v_y, v_z along the Y axis (right plot in Fig 3.28) indicates an unstable equilibrium in this central region. However, the velocity components along the X-axis are stronger and expected to be dominant in controlling particle dynamics. Collectively, it can be understood that a stable particle assembly can be formed in the common centre where there is no excitation spot, majorly due to the complex fluid flow profile in such a system.

3.2.5 Thermoelectric trapping

Largescale assembly of plasmonic nanoparticles has a direct consequence of being able to produce very enhanced and localised electric fields. To be able to harness this effect, we need to ensure that the assembled AuNPs overlap with the surface plasmon fields, that is, they are very close to the Au film surface. Since the SP fields are evanescent fields, they decay exponentially away from the surface. For SP generated at the water-glass interface,

having refractive indices n_s and n_c respectively can be calculated as [45],

$$d_p = \beta^{-1} = \frac{\lambda}{2\pi \left[(n_c \sin\theta_{\mathrm{SP}})^2 - n_s^2 \right]^{1/2}} \tag{3.16}$$

Which comes out to be $d_p \sim 130$ nm. Thus, if the AuNP is farther beyond this penetration depth, there will not be significant field enhancement due to insufficient overlap between the particle volume and the SP field. To excite the localised surface plasmons (LSP) of the AuNP, it is necessary that the particles are as close to the Au surface as possible so that they overlap with the evanescent SP fields. Apart from the random Brownian motion of the AuNP, which causes fluctuation in the particle-surface distance, the out-of-plane fluidic force pulls the AuNP upwards as it approaches the excitation spot. This increasing particle-surface distance prevents the excitation of LSP of AuNP. To achieve field enhancement, we must overpower the out-of-plane fluidic forces so that the particles remain close to the excitation spot.

For this purpose, we utilise the principle of thermoelectric trapping. Consider an ionic solution containing negative and positive ions. Under a thermal gradient, temperature-dependent ionic mobility can lead to a spatial separation of ions in the solution, which can activate an electrostatic field. Depending on the charge of a suspended particle in the solution, it can be driven under the influence of this temperature-mediated electric field or thermoelectric field [46]. For our experiment, we use the surfactant cetyltrimethylammonium chloride or CTAC in short. The working principle when using CTAC is depicted in Fig 3.29 [17] and can be explained as: CTAC can separate into a positive CTA^+ ion and a negative chloride (Cl^-) ion. The CTA^+ cations can adsorb to a particle's surface and make the particle positively charged. Above a critical micelle concentration of 0.13 mM, the CTA^+ cations can self-assemble into micelles to form macro-cations. In the absence of a temperature gradient, the macrocations, Cl^- anions, and positively charged particles are randomly dispersed in the solution. However, under a thermal gradient, the ions move differently owing to their different Soret coefficients, which is the ratio of particle thermal diffusivity to particle's ordinary diffusivity D_T/D. The Soret coefficient of both Cl ions ($7.18 \times 10^{-4} K^{-1}$) and $CTAC$ micelles ($10^{-2} K^{-1}$) is positive, meaning they will migrate from the hot to the cold region. But, since the Soret coefficient of Cl^- ions is much lower than that of CTA^+ ions, they have a smaller thermodiffusivity than the micellar macrocations. This causes the micelles to migrate towards the colder region quickly and lead to a spatial separation of the ions, such that the ion flux is a balance between the concentration gradient and thermal gradient in the steady state. The resultant electric field due to such a spatial ionic separation is [21],

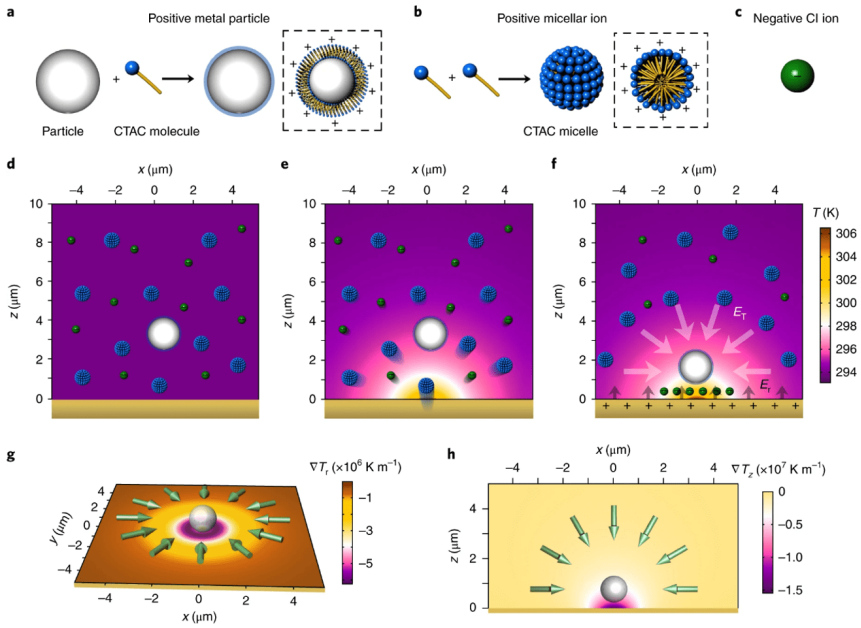

Figure 3.29: Schematic explaining the principle of optothermoelectric trapping [17].

$$E_T = \frac{k_B T \nabla T}{e} \frac{\sum_i Z_i c_i S_{Ti}}{\sum_i Z_i^2 c_i} \tag{3.17}$$

Where i indicates the ionic species, that is, CTA^+ micellar ions or Cl ions, k_B is the Boltzmann constant, T is the environmental temperature, ∇T is the temperature gradient, e is the elemental charge, and Z_i, c_i and S_{Ti} are the charge number, the concentration and the Soret coefficient of the i^{th} ionic species, respectively. We obtain a resultant electric field pointing towards the temperature hotspot. Any positively charged particle will be pushed towards the hotspot under the influence of the electrostatic field. The corresponding thermoelectric force can be calculated from the zeta potential ζ of the particle in the given CTAC concentration c as,

$$F_{T,E} = \int_S \sigma E_T dA \tag{3.18}$$

Where σ is the effective surface charge density of the particle. When the optical illumination mediates the required temperature gradient in this mechanism, then this trapping method is termed optothermoelectric trapping. The electrostatic force can act against the out-of-plane fluidic force in our system and trap the AuNP close to the temperature hotspot, that is, the Au surface.

To apply this technique to our system, we add 5 mM CTAC to the 400 nm diameter AuNP solution and repeat the experiment, keeping everything else the same. Fig 3.30 shows the

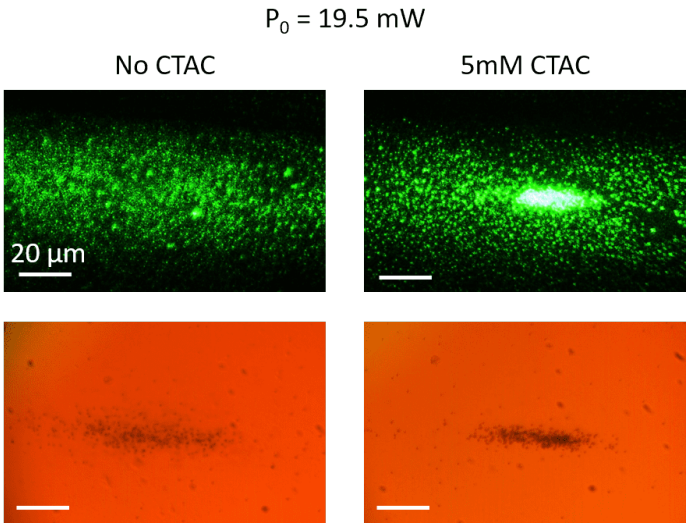

Figure 3.30: Assembly of 400 nm diameter AuNP formed and the field enhancement obtained in the presence and absence of 5 mM CTAC.

bright and dark field images of the assembled AuNP at a power of $\sim$ 20mW. In the absence of CTAC, the AuNPs are accumulated and still trapped at the hotspot. But in the dark field, no field enhancement is observed, as also shown in previous sections. In the presence of CTAC, a closely packed assembly of particles is formed, giving a multifold intensity enhancement. This enhancement indicates that not only are the particles very close to each other, but they are also very close to the Au surface, which enables their overlap with the surface plasmon fields and excitation of their LSPs. This is the effect of the thermoelectric force against the out-of-plane fluidic forces.

To get an estimate of the order of magnitude of the thermoelectric force compared to the other optical and fluidic forces in the system, we calculated the thermoelectric force using the temperature gradient as computed by COMSOL. In the equation for thermoelectric field Eq 3.17, let subscript 1 denote CTA^+ micelles and 2 denote Cl^- ions. Then, $Z_1 = +1, Z_2 = -1, n_1 = 5/89$ mM, $n_2 = 5$ mM, S_{T1} and S_{T2} are as mentioned above, and $T\nabla T$ is as computed from the temperature profile obtained in COMSOL (p-polarised temperature profile in Fig 3.13). Once we have the electrostatic field, we will need the total surface charge on the AuNP to calculate the thermoelectric force. For a charged particle whose zeta potential is known, the surface charge density is given as follows [47]:

$$\sigma = \frac{\varepsilon_r \varepsilon_0 k_B T}{e} \left[exp\left(\frac{e\zeta}{2k_B T}\right) - exp\left(-\frac{e\zeta}{2k_B T}\right) + \frac{4}{\kappa a} \cdot \frac{exp(e\zeta/2k_B T) - 1}{exp(e\zeta/2k_B T) + 1} \right] \tag{3.19}$$

$$\kappa = \sqrt{\frac{2Ie^2}{\varepsilon_r \varepsilon_0 k_B T}} \tag{3.20}$$

Where e is the elementary charge, T is the absolute temperature, k_B is the Boltzmann constant, ζ is the zeta potential, ε_r is the relative permittivity of the solution, ε_0 is the permittivity of vacuum, η is the viscosity of the solution, κ is the inverse Debye length, N is Avogadro's number, a is the particle radius, I is the ionic concentration in number/m^3 given as

$$I = \frac{1}{2}\sum_{i=1}^{n} c_i z_i^2 \tag{3.21}$$

Where c_i is the molar concentration of ion i and z_i is its charge number. A factor of half is included since both cations and anions are considered.

For our calculations, we have used a CTAC concentration of 5 mM. According to previous reports [17], an AuNP of diameter upto 200 nm dispersed in such a concentration gets positively charged with a zeta potential of up to $\sim$ 73 mV. Here, since the size of AuNP used in our work is 400 nm, we expect its zeta potential to be slightly greater and thus approximate a value of 80 mV to get an estimate of the order of thermoelectric forces. Using these parameters, we obtain the surface charge density σ on a 400 nm diameter AuNP in a 5 mM CTAC solution. Thus, the total surface charge will be $Q = 4\pi r^2 \cdot \sigma$ and the force can be calculated as $F_{ET} = Q \cdot E_T$. Note that since the surface charge depends exponentially on the zeta potential, the thermoelectric force calculated here is, at its best, an underestimation. The simulated thermolectric force profile along the X-axis, 50 nm above the Au surface, is as shown in Fig 3.31, for a maximum temperature increment of 50K.

Notice the order of magnitude of the thermoelectric forces, going up to nN compared to the sub-pN fluidic forces. This indicates that the thermoelectric forces can successfully overpower the out-of-plane fluidic forces and effectively press the AuNP close to the hotspot, that is, the excitation spot. Also, since the thermoelectric force acts radially inwards, it also supports the in-plane fluidic forces and enables tight packing of the assembled particles, as is visible in Fig 3.30. Collectively, the AuNP are packed closer to each other and in near proximity to the surface plasmon fields, leading to a multifold intensity enhancement, as is visible from the CCD images as well.

To test the applicability of this method, the experiment was repeated with smaller AuNP as well, of diameters 150 nm and 250 nm, keeping the CTAC concentration constant at 5 mM. It is observed that 250 nm AuNPs are also stably trapped in the presence of CTAC, as

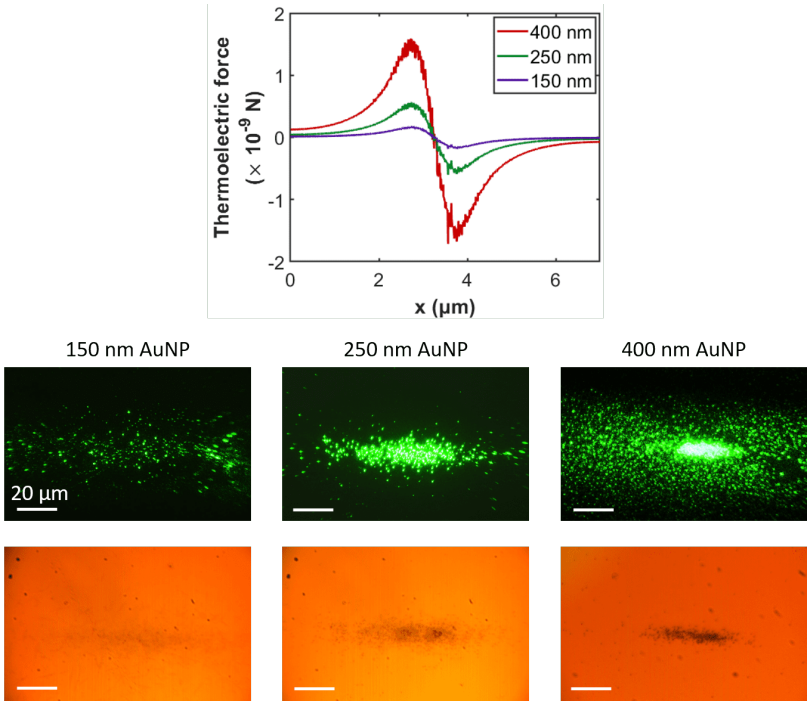

Figure 3.31: The plot shows the thermoelectric force for different sized AuNP subjected to a temperature gradient as shown in Fig 3.13. The bottom panel shows the experimental images of the field enhancement and assembly of AuNP obtained in the presence of 5 mM CTAC at power $\sim$ 20 mW.

shown in Fig 3.31. Although not clearly visible in the figure, 150 nm AuNP also assemble in the presence of CTAC but their Brownian motion is still strong due to which they are not closely confined to the surface.

Simulations were also repeated for 250 nm and 150 nm AuNP to calculate the fluidic and thermoelectric forces. To reaffirm the negligible effect of optical forces, the total electric field was computed by placing the particle in the centre of the excitation spot, in the same geometry dimensions as used previously for optical force simulation. The optical force was estimated by integrating the Maxwell stress tensor and came out to be of the order of $10^{-20} - 10^{-21}$ for 250 nm and 150 nm AuNP, compared to $10^{-19} - 10^{-20}$ for 400 nm AuNP. The fluidic forces are as shown in the previous section.

Fluorescence of R6G: a comparison of intensity enhancement

To quantify and verify the intensity enhancement due to SP and LSP fields of the Au film and AuNP, respectively, we added 1 μM of Rhodamine 6G to the sample solution of 400 nm AuNP and recorded the photoluminescence spectra from the assembly of particles formed

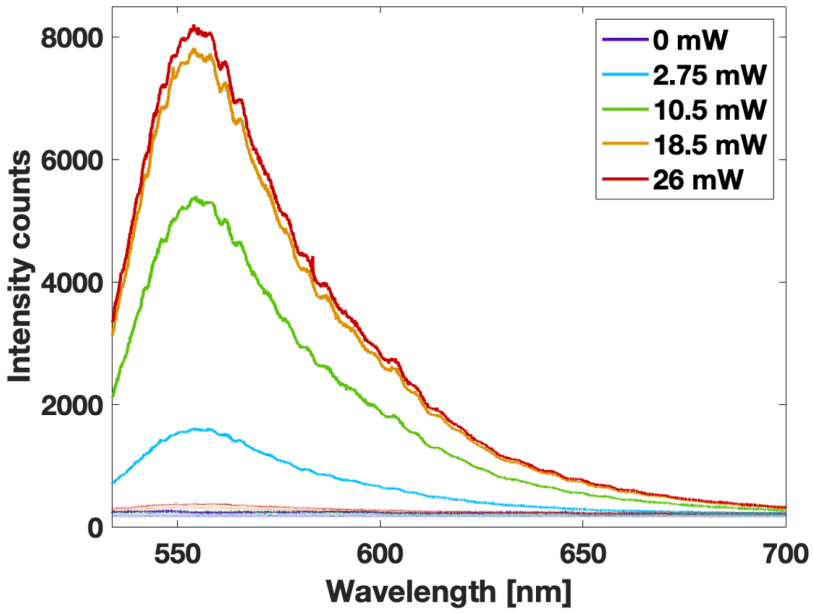

Figure 3.32: Photoluminescence spectra of 1 μM Rhodamine 6G solution taken from an assembly of 400 nm AuNP, in the presence (dark line plots) and absence (faint line plots) of 5 mM CTAC.

at different powers. Rhodamine 6G is a fluorescent dye with an excitation peak at 524 nm and emission peak at 548 nm. The experiment was repeated by adding same amount of rhodamine 6G to the sample solution containing 5 mM CTAC. Again, the photoluminescence spectra were recorded from the dense particle assemblies at different powers. A comparison of the spectra recorded from particle assemblies in the presence and absence of CTAC is as shown in Fig 3.32. The dark solid lines represent the spectra recorded in the presence of CTAC, going up to 8000 intensity counts at the maximum power of our system. The faint lines at the bottom of the plot with very small intensity counts of up to 400 correspond to the spectra recorded in the absence of CTAC. Thus, the addition of CTAC-facilitated thermoelectric effects leads to an intensity rise of over 20 times. This is a consequence of closed packing of AuNP and their close proximity to the surface plasmon fields.

3.3 Brownian dynamics in Evanescent field

It has been established that an electromagnetic wave can exert force on a micro/nanoparticle. Particles lying in this size range are Brownian in nature, meaning they perform random motion due to molecular collisions in the medium of suspension. This Brownian motion can be manipulated by guiding the particle using structured optical forces. Such forces can be generated by using patterned electromagnetic waves, for example standing waves [48]. Evanescent waves are also an instance of structured surface waves that propagate along an

Table 3.2: Parameters used in Matlab Brownian motion simulations

Parameter	Notation	Value
Refractive index of water	n_2	1.33
Refractive index of glass	n_1	1.75
Refractive index of particle	n_p	1.59
Wavelength	λ	500 or 1000 nm
Frequency	ω	$2\pi c/\lambda$
Waist radius	w_0	1 µm
Particle radius	a	100 nm
Rayleigh range	z_0	$\pi w_0^2/\lambda$
Free space permeability	μ_0	$4\pi \times 10^{-7}$ [m.kg/s^2.A^2]
Free space permittivity	ε_0	8.85×10^{-12} [C^2/Nm^2]
Relative permittivity of particle	ε_r	n_p^2 [C^2/Nm^2]
Relative permittivity of water	ε_w	1.8 [C^2/Nm^2]
Viscosity of water	η	0.001 [kg/m.s]
Extinction cross-section of partcle	σ	$k * \alpha''/\varepsilon_0$
Temperature	T	300 K
Boltzmann constant	k_B	1.38×10^{-23}
Electric field magnitude	E_0	$2P/\pi w_0^2$ [V/m]
Power	P	200 mW
Speed of light	c	3×10^8 [m/s]

interface and decay perpendicular to it [49]. As described in the methods in Chapter 2, evanescent waves are simulated in Matlab. The parameters used are as listed in Table 3.2. Consider an electromagnetic wave having Gaussian intensity envelope. When this wave hits an interface, it can get either reflected or transmitted or both, depending on the angle of incidence and properties of the interface.

We start by simulating a normal propagating Gaussian electromagnetic wave in air, travelling along Z-axis. Recall (from Chapter 1) the electric field expression as,

$$E(\rho,z) = E_0 \frac{w_0}{w(z)} e^{-\frac{\rho^2}{w(z)^2}} e^{-ikz - i\zeta(z) + ik\frac{\rho^2}{2R(z)}} \tag{3.22}$$

Here, we need to note that the wave is travelling along the Z-axis and the intensity distribution is Gaussian in the perpendicular XY-plane. This simply gives $\vec{k} \cdot \vec{r} = (k_x\hat{x} + k_y\hat{y} + k_z\hat{z}) \cdot (x\hat{x} + y\hat{y} + z\hat{z}) = kz$, since $\vec{k} = k_z\hat{z}$. The first exponential determines the intensity magnitude and its distribution in the perpendicular XY-plane. Thus, the field is written in cylindrical

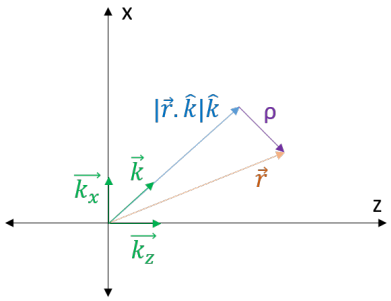

Figure 3.33: Wavevector pointing in an arbitrary direction in the XZ-plane, having components $\vec{k_x}$ and $\vec{k_z}$ along the X- and Z-axes. Intensity is to be calculated at a point $\vec{r}$.

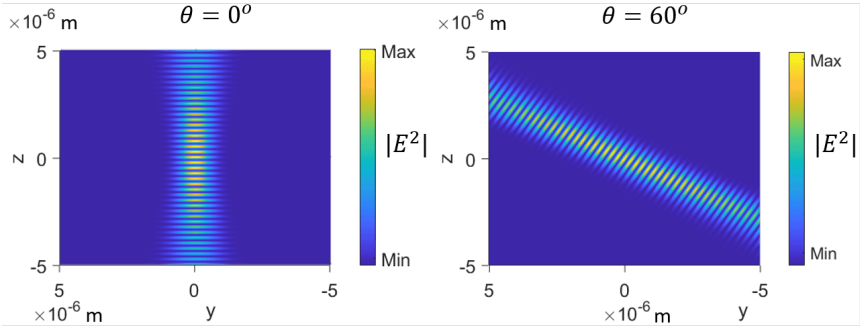

Figure 3.34: Intensity plot of a Gaussian electromagnetic wave propagating at angle θ with respect to the z-axis.

coordinates oriented along the propagation direction. Simulating in Matlab, the intensity envelope obtained is as shown in Fig 3.34 (left) for $\theta = 0^o$. But if the wave is not travelling along the Z-axis, then $\vec{k}$ also has other components. Consider if the wave is travelling in the XZ-plane, making an angle θ with the Z-axis, as shown in Fig 3.33. Then the wave vector will be written as,

$$\vec{k} = kcos\theta\hat{k} + ksin\theta\hat{i} \tag{3.23}$$

ρ will not be in the xy-plane anymore. As shown in Fig 3.33, it will now span the 3D space and will be a function of x, y, z. From the figure it can be understood,

$$\rho = \vec{r} - |\vec{r}\cdot\hat{k}|\hat{k} \tag{3.24}$$

Where,

$$|\vec{r}\cdot\hat{k}|\hat{k} = (x\hat{x} + y\hat{y} + z\hat{z})\cdot(ksin\theta\hat{x} + kcos\theta\hat{z})\frac{ksin\theta\hat{x} + kcos\theta\hat{z}}{k^2cos^2\theta + k^2sin^2\theta} \tag{3.25}$$

Upon simplifying we get,

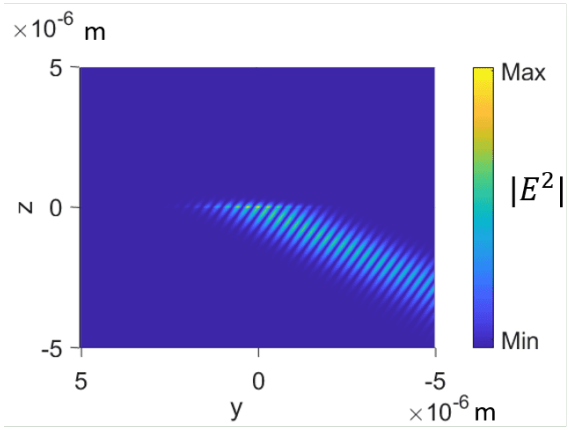

Figure 3.35: Intensity plot of a Gaussian electromagnetic wave incident at glass ($z < 0$)-water ($z > 0$) interface at angle $\theta = 60^o$

$$\rho = cos\theta(xcos\theta - zsin\theta)\hat{x} + y\hat{y} + sin\theta(zsin\theta - xcos\theta)\hat{k} \tag{3.26}$$

Using the above mentioned ρ and $\vec{k}$, we simulate an obliquely travelling Gaussian envelope electromagnetic wave which looks like that in Fig 3.34 (right), when oriented at an angle 60^o. Now, to classify the space into two media, we assign a refractive index n_1 to space with $z < 0$ and refractive index n_2 to space with $z > 0$, such that $n_1 > n_2$. This is included in the form of an *if* loop into the Matlab program. Using the evanescent wave equations as derived in Chapter 2 and substituting the Gaussian electric field with updated $\vec{k}$ and ρ, we simulate the evanescent wave at glass ($n_1 = 1.75$)-water ($n_2 = 1.3$) interface as shown in Fig 3.35.

As described in Chapter 2, from the electric and magnetic fields, we calculate the poynting vector of the evanescent field in medium 2, that is, $z > 0$. Armed with the electromagnetic fields information for the evanescent wave, the optical forces are calculated directly from Eq 2.34 and 2.35. Substituting it into the overdamped Langevin equation Eq 2.38, we simulated the Brownian trajectory of a SiO_2 nanosphere (SiNP) having radius 100 nm. As a boundary condition for the interface, whenever the particle centre coordinate (x_p, y_p, z_p) is such that $z_p < 0$, then its z_p coordinate is replaced by a; and whenever $z_p > 0$ but $< a$. then again z_p is adjusted to a. The wavelength of the incident wave is taken as 1000 nm so that $a << \lambda$ can be taken as a dipolar approximation. The Brownian dynamics can be seen in Fig 3.36. It does not seem that the Brownian motion of SiNP is affected by the evanescent field. This is because, the order of optical forces for such a small volume particle is very small, compared to the random forces. To see the effect of the forces, we increased the order of optical forces by 2 orders and computed the Brownian motion again, as shown in Fig 3.37.

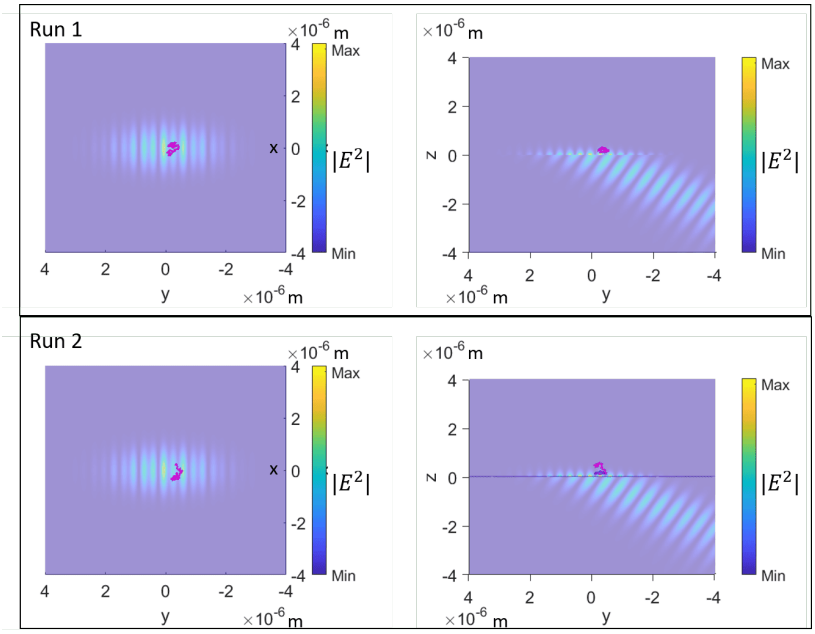

Figure 3.36: Brownian motion of a SiNP of radius 100 nm under the evanescent field produced by total internal reflection of a Gaussian wave ($\lambda = 1000$ nm). Results from two separate runs of the program are shown here, depicting the XY- and YZ-profiles.

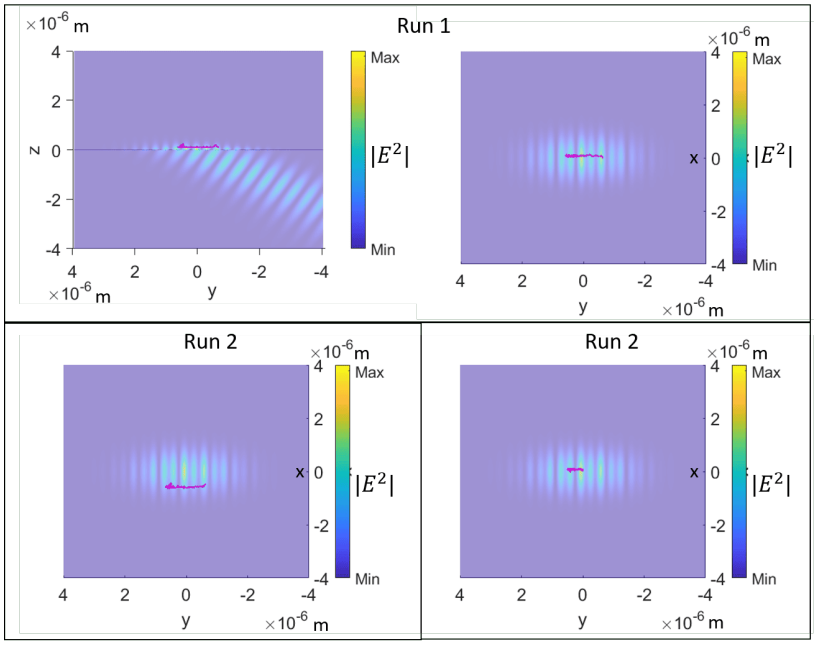

Figure 3.37: Brownian motion of SiNP when the optical forces are increased by 2 orders of magnitude. Results from three separate runs of the program are shown here, with different initial positions of the particle to start with.

As can be seen, the particle exhibits directed motion along the propagation direction of the evanescent wave. This is in direct correspondence to the experimental observation of [49] [45].

Chapter 4

CONCLUSIONS AND FUTURE DIRECTIONS

In this work, we have studied the mechanism for the formation of reversible particle assemblies using evanescently excited plasmonic fields. The significance of the role of plasmons and fluid flow is studied in detail in such ”plasmofluidic” traps. The relative strength of these forces is quantified and compared using FEM simulations. We show that optical forces play a negligible role in such largescale particle manipulation. The slip fluid flow and viscous forces exerted by it are the major players which lead to nanoparticle assembly formation. The magnitude of these forces and flows can be directly controlled by tuning the temperature via the incident power. An approximate calibration between the incident power and temperature rise is drawn using the phase transition of 5CB liquid crystal. The effect of temperature-controlled fluid flow on the nanoparticle assembly is also shown. Fluid flow at high temperatures is too strong to allow a stable particle assembly. Convective fluid flows in our system have been shown to be greatly suppressed and weak compared to slip fluid flows. The corresponding convective viscous forces are also found to be too small and comparable to the order of optical forces.

Using our understanding of the role of fluid flow in nanoparticle dynamics, we have attempted to explain the pattern formation of nanoparticles as observed in our lab previously under similar experimental conditions. A complex fluid flow emerging due to multiple temperature hotspots leads to particle accumulation in places where no direct excitation exists. It is observed that despite the strong viscous forces, the intensity enhancement due to such a plasmonic nanoparticle assembly is very poor. It is explained how the fluid forces are again responsible for not allowing the nanoparticles to come close to the surface fields. We then moved on to utilise the thermoelectric effects to act against the fluid flow, by adding small concentrations of surfactant CTAC. Experimentally it has been shown that thermo-

electric forces greatly enable the close packing of nanoparticles in the assembly, bringing them closer to the Au film and resulting in multifold intensity enhancement. A comparison has been drawn between intensity in the presence and absence of the thermoelectric effects. Also, smaller nanoparticles which were not trapped earlier by plasmofludic forces, are effectively trapped with the aid of thermoelectric forces. To compare the intensity enhancement, photoluminescence of Rhodamine 6G is captured in the presence and absence of CTAC and an intensity increase of 20 times is recorded. Towards the end, we briefly look at the Brownian motion of a nanoparticle under the influence of evanescent optical forces, which exhibits a directed motion along the propagation of evanescent waves.

The tightly packed assembly of plasmonic particles formed under the aid of thermoelectric effects results in large scattering of the surface fields. One of the future directions of this work is to study the scattered light from such tightly packed plasmonic assemblies. Interestingly, when this scattered light is visualised in the Fourier plane, a dark band of intensity is seen. This dark band is visible only when the particles are plasmonic and close to each other. In the absence of CTAC, the loose assembly does not exhibit any such feature in the Fourier plane. A possible origin of this is the LSP of the particles, which is excited only when they are close to the Au surface, that is, in the presence of CTAC. This problem is currently under investigation. If the scattering signature from such plasmonic assemblies does carry some unique feature, then it will also be very compelling to perform the experiment in the presence of monolayer of 2D materials and observe their Raman and photoluminescence signals, which can carry some possible directional properties. Another obvious application of such field-enhancing structures is biosensing and single molecule detection. Since very low CTAC concentration can result in large field multiplication at relatively lower powers, one should be able to perform single molecule detection at lower powers and possibly lower concentrations of molecules as well. By increasing the surfactant concentration, we expect to form tighter assemblies at very lower powers, which can still give sufficient intensity enhancement. This is a hypothesis which is also under investigation.

To talk about the challenges in this work, as emphasised above, temperature distribution is a key factor in assembly formation. Thus, precise estimation of temperature is crucial to correctly quantify the effects of the thermal field. As mentioned in the text, the phase transition method is, at its best, an underestimation of the temperature, and more accurate measurements should be performed. The pattern formation by nanoparticles as mentioned above, was not observed with the AuNP used in this work. We tried to replicate similar experimental conditions, but no patterns were formed. This indicates a possible role of

the interparticle interactions, surface properties of the particles and scale of the fluid flow (much larger in the case of pattern-forming experiments). While the forces were quantified using simulations, an experimental quantification can also be attempted by employing particle tracking and particle velocimetry. This can give an experimental confirmation of the fluidic and thermoelectric forces in the system. However, due to the large experimental area, it is difficult to track AuNP under the small viewing area of a high-magnification objective lens. On the other hand, a low-magnification lens will provide a larger viewing area to observe the entire extent of the phenomenon, but one will not be able to trace individual nanoparticle dynamics.

Thus, the detailed study of the mechanisms of large-scale assembly formation of very small nanoparticles gives an insight into the interplay of multiple fields and their control parameters. Such a deeper understanding will enable finer manipulation of different types of particles at different working scales. While plasmofluidic trapping and thermoelectric effects have been studied in great detail over the last few years, through this work, we have tried to draw a coherent comparison between them, understanding the complex interplay leading to large-scale manipulation of colloidal dynamics.

Bibliography

[1] Peter Mörters and Yuval Peres. *Brownian motion*, volume 30. Cambridge University Press, 2010.

[2] Giovanni Volpe, Onofrio M Maragò, Halina Rubinsztein-Dunlop, Giuseppe Pesce, Alexander B Stilgoe, Giorgio Volpe, Georgiy Tkachenko, Viet Giang Truong, Síle Nic Chormaic, Fatemeh Kalantarifard, et al. Roadmap for optical tweezers. *Journal of Physics: Photonics*, 5(2):022501, 2023.

[3] Martin Fränzl and Frank Cichos. Hydrodynamic manipulation of nano-objects by optically induced thermo-osmotic flows. *Nature communications*, 13(1):656, 2022.

[4] Mariko Suga, Saori Suda, Masatoshi Ichikawa, and Yasuyuki Kimura. Self-propelled motion switching in nematic liquid crystal droplets in aqueous surfactant solutions. *Physical Review E*, 97(6):062703, 2018.

[5] Vandana Sharma, Diptabrata Paul, Shailendra K Chaubey, Sunny Tiwari, and GV Pavan Kumar. Large-scale optothermal assembly of colloids mediated by a gold microplate. *Journal of Physics: Condensed Matter*, 32(32):324002, 2020.

[6] Partha Pratim Patra, Rohit Chikkaraddy, Ravi PN Tripathi, Arindam Dasgupta, and GV Pavan Kumar. Plasmofluidic single-molecule surface-enhanced raman scattering from dynamic assembly of plasmonic nanoparticles. *Nature communications*, 5(1):4357, 2014.

[7] Partha Pratim Patra, Rohit Chikkaraddy, Sreeja Thampi, Ravi PN Tripathi, and GV Pavan Kumar. Large-scale dynamic assembly of metal nanostructures in plasmofluidic field. *Faraday discussions*, 186:95–106, 2016.

[8] WE Uspal. Theory of light-activated catalytic janus particles. *The Journal of Chemical Physics*, 150(11), 2019.

[9] Maurizio Righini, Anna S Zelenina, Christian Girard, and Romain Quidant. Parallel and selective trapping in a patterned plasmonic landscape. *Nature Physics*, 3(7):477–480, 2007.

[10] Ashish Yadav, Burak Gerislioglu, Arash Ahmadivand, Ajeet Kaushik, Gary J Cheng, Zhengbiao Ouyang, Qing Wang, Vikram Singh Yadav, Yogendra Kumar Mishra, Yongling Wu, et al. Controlled self-assembly of plasmon-based photonic nanocrystals for high performance photonic technologies. *Nano Today*, 37:101072, 2021.

[11] Sunny Tiwari, Utkarsh Khandelwal, Vandana Sharma, and GV Pavan Kumar. Single molecule surface enhanced raman scattering in a single gold nanoparticle-driven thermoplasmonic tweezer. *The Journal of Physical Chemistry Letters*, 12(49):11910–11918, 2021.

[12] Santosh Yadav, Ashwani Kumar Sharma, and Pradeep Kumar. Nanoscale self-assembly for therapeutic delivery. *Frontiers in Bioengineering and Biotechnology*, 8:127, 2020.

[13] William L Barnes, Alain Dereux, and Thomas W Ebbesen. Surface plasmon subwavelength optics. *nature*, 424(6950):824–830, 2003.

[14] Eric Busseron, Yves Ruff, Emilie Moulin, and Nicolas Giuseppone. Supramolecular self-assemblies as functional nanomaterials. *Nanoscale*, 5(16):7098–7140, 2013.

[15] Neda Habibi, Nazila Kamaly, Adnan Memic, and Hadi Shafiee. Self-assembled peptide-based nanostructures: Smart nanomaterials toward targeted drug delivery. *Nano today*, 11(1):41–60, 2016.

[16] Diptabrata Paul, Rahul Chand, and GV Pavan Kumar. Optothermal evolution of active colloidal matter in a defocused laser trap. *ACS Photonics*, 9(10):3440–3449, 2022.

[17] Linhan Lin, Mingsong Wang, Xiaolei Peng, Emanuel N Lissek, Zhangming Mao, Leonardo Scarabelli, Emily Adkins, Sahin Coskun, Husnu Emrah Unalan, Brian A Korgel, et al. Opto-thermoelectric nanotweezers. *Nature photonics*, 12(4):195–201, 2018.

[18] Diptabrata Paul, Desmond Quinn, and Frank Cichos. Opto-thermal assembly of three-dimensional photonic crystals. In *Optical Trapping and Optical Micromanipulation XX*, page PC1264913. SPIE, 2023.

[19] Kai Wang, Ethan Schonbrun, Paul Steinvurzel, and Kenneth B Crozier. Trapping and rotating nanoparticles using a plasmonic nano-tweezer with an integrated heat sink. *Nature communications*, 2(1):469, 2011.

[20] V Garcés-Chávez, Kishan Dholakia, and GC Spalding. Extended-area optically induced organization of microparticles on a surface. *Applied Physics Letters*, 86(3), 2005.

[21] Ashutosh Shukla, Sunny Tiwari, Ayan Majumder, Kasturi Saha, and GV Pavan Kumar. Optothermal trapping of fluorescent nanodiamonds using a drop-casted gold nanoparticle. *arXiv preprint arXiv:2210.02874*, 2022.

[22] Jingang Li, Linhan Lin, Yuji Inoue, and Yuebing Zheng. Opto-thermophoretic tweezers and assembly. *Journal of Micro-and Nano-Manufacturing*, 6(4):040801, 2018.

[23] Frederique De Fornel. *Evanescent waves: from Newtonian optics to atomic optics*, volume 73. Springer Science & Business Media, 2001.

[24] Stefan A Maier et al. *Plasmonics: fundamentals and applications*, volume 1. Springer, 2007.

[25] Akihiro Sato. Surface plasmon fluorescence spectroscopy and optical waveguide fluorescence spectroscopy in limit of detection studies. *Max Planck Institute for Polymer Research, Johannes Gutenberg University of Mainz, Mainz. Master Thesis*, 2006.

[26] William L Barnes. Surface plasmon–polariton length scales: a route to subwavelength optics. *Journal of optics A: pure and applied optics*, 8(4):S87, 2006.

[27] Philip Jones, Onofrio Maragó, and Giovanni Volpe. *Optical tweezers*. Cambridge University Press Cambridge, 2015.

[28] Holger Kress, Ernst HK Stelzer, and Alexander Rohrbach. Measuring and adjusting the trapping position in optical tweezers. In *DGaO Proceedings*. DGaO, 2005.

[29] Guillaume Baffou and Romain Quidant. Thermoplasmonics. In *World Scientific Handbook of Metamaterials and Plasmonics: Volume 4: Recent Progress in the Field of Nanoplasmonics*, pages 379–407. World Scientific, 2018.

[30] Zhihan Chen, Jingang Li, and Yuebing Zheng. Heat-mediated optical manipulation. *Chemical reviews*, 122(3):3122–3179, 2021.

[31] Manuel G Velarde and Christiane Normand. Convection. *Scientific American*, 243(1):92–109, 1980.

[32] Franz M Weinert and Dieter Braun. Observation of slip flow in thermophoresis. *Physical review letters*, 101(16):168301, 2008.

[33] David J Griffiths. *Introduction to electrodynamics*. Cambridge University Press, 2023.

[34] Vandana Sharma, Sunny Tiwari, Diptabrata Paul, Ratimanasee Sahu, Vijayakumar Chikkadi, and GV Pavan Kumar. Optothermal pulling, trapping, and assembly of colloids using nanowire plasmons. *Soft Matter*, 17(48):10903–10909, 2021.

[35] Roberto Piazza and Alberto Parola. Thermophoresis in colloidal suspensions. *Journal of Physics: Condensed Matter*, 20(15):153102, 2008.

[36] Jiaojiao Hua, Fan Wu, Fengru Fan, Wenhui Wang, Zhongfeng Xu, and Fuli Li. Synthesis and surface plasmonic properties of ultra-thick silver nanowires. *Journal of Physics: Condensed Matter*, 28(25):254005, 2016.

[37] Jiri Homola and M Piliarik. Springer series on chemical sensors and biosensors, 2006.

[38] Rahul Chand, Chaudhary Eksha Rani, Diptabrata Paul, and GV Pavan Kumar. Emergence of directional rotation in an optothermally activated colloidal system. *ACS Photonics*, 10(11):4006–4013, 2023.

[39] Andreas P Bregulla, Alois Würger, Katrin Günther, Michael Mertig, and Frank Cichos. Thermo-osmotic flow in thin films. *Physical review letters*, 116(18):188303, 2016.

[40] Alois Würger. Thermal non-equilibrium transport in colloids. *Reports on Progress in Physics*, 73(12):126601, 2010.

[41] S Iacopini, Roberto Rusconi, and Roberto Piazza. The "macromolecular tourist": Universal temperature dependence of thermal diffusion in aqueous colloidal suspensions. *The European Physical Journal E*, 19:59–67, 2006.

[42] Marcel Giesbers, J Mieke Kleijn, and Martien A Cohen Stuart. The electrical double layer on gold probed by electrokinetic and surface force measurements. *Journal of colloid and interface science*, 248(1):88–95, 2002.

[43] Faith A Morrison. *An introduction to fluid mechanics*. Cambridge University Press, 2013.

[44] Alois Würger. Thermophoresis in colloidal suspensions driven by marangoni forces. *Physical review letters*, 98(13):138301, 2007.

[45] Giovanni Volpe, Romain Quidant, Gonçal Badenes, and Dmitri Petrov. Surface plasmon radiation forces. *Physical review letters*, 96(23):238101, 2006.

[46] Linhan Lin, Xiaolei Peng, Mingsong Wang, Leonardo Scarabelli, Zhangming Mao, Luis M Liz-Marzán, Michael F Becker, and Yuebing Zheng. Light-directed reversible assembly of plasmonic nanoparticles using plasmon-enhanced thermophoresis. *ACS nano*, 10(10):9659–9668, 2016.

[47] K Ohsawa, M Murata, and H Ohshima. Zeta potential and surface charge density of polystyrene-latex; comparison with synaptic vesicle and brush border membrane vesicle. *Colloid and Polymer Science*, 264:1005–1009, 1986.

[48] Silvia Albaladejo, Manuel I Marqués, Frank Scheffold, and Juan Jose Sáenz. Giant enhanced diffusion of gold nanoparticles in optical vortex fields. *Nano letters*, 9(10):3527–3531, 2009.

[49] Satoshi Kawata and Tadao Sugiura. Movement of micrometer-sized particles in the evanescent field of a laser beam. *Optics letters*, 17(11):772–774, 1992.